

NASA CONTRACTOR REPORT

NASA CR-2055



NASA CR-2055

0061159

TECH LIBRARY KAFB, NM

LOAN COPY: RETURN TO
AFWL (DOUL)
KIRTLAND AFB, N. M.

MAGNETIC PERTURBATION INSPECTION OF INNER BEARING RACES

by John R. Barton and James Lankford

Prepared by

SOUTHWEST RESEARCH INSTITUTE

San Antonio, Texas 78284

for Lewis Research Center

NATIONAL AERONAUTICS AND SPACE ADMINISTRATION • WASHINGTON, D. C. • MAY 1972



0061159

1. Report No. CR-2055		2. Government Accession No.		3. Recipient's Catalog No.	
4. Title and Subtitle MAGNETIC PERTURBATION INSPECTION OF INNER BEARING RACES				5. Report Date May 1972	
				6. Performing Organization Code	
7. Author(s) John R. Barton and James Lankford				8. Performing Organization Report No. SwRI 15-2773	
9. Performing Organization Name and Address Southwest Research Institute San Antonio, Texas 78284				10. Work Unit No.	
				11. Contract or Grant No. NAS 3-13944	
12. Sponsoring Agency Name and Address National Aeronautics and Space Administration Washington, D. C. 20546				13. Type of Report and Period Covered Contractor Report	
				14. Sponsoring Agency Code	
15. Supplementary Notes Project Manager, Richard J. Parker, Fluid System Components Division, NASA Lewis Research Center, Cleveland, Ohio					
16. Abstract Approximately 100 inner race bearings were inspected nondestructively prior to endurance testing. Two of the bearings which failed during testing spalled at the sites of subsurface inclusions previously detected by using magnetic field perturbation. At other sites initially judged to be suspect, subsurface inclusion-nucleated cracking was observed. Inspection records and metallurgical sectioning results are presented and discussed.					
17. Key Words (Suggested by Author(s)) Nondestructive evaluation Cracks Fatigue Spalling Inclusions Bearings				18. Distribution Statement Unclassified - unlimited	
19. Security Classif. (of this report) Unclassified		20. Security Classif. (of this page) Unclassified		21. No. of Pages 63	
				22. Price* \$3.00	

* For sale by the National Technical Information Service, Springfield, Virginia 22151

Bearings - nondestructive testing
2. Fatigue (materials)

TABLE OF CONTENTS

	<u>Page</u>
I. INTRODUCTION	1
A. Background	1
B. Description of Magnetic Method	1
C. Bearing Fatigue Tests	4
D. Metallurgical Investigation	7
II. DATA SUMMARY AND ANALYSIS	8
A. Test Bearings	8
B. Inspections	8
C. Records and Data Tabulation	12
D. Metallurgical Investigation	21
III. ANALYSIS	47
A. Pre-Endurance Testing Data Analysis	47
B. Post-Endurance Testing Data Analysis	49
IV. CONCLUSIONS	57

LIST OF FIGURES

<u>Figure</u>	<u>Title</u>	<u>Page</u>
1	Perturbations in Magnetic Flux Caused by Inclusion in Ferromagnetic Material	2
2	Flux Sensitive Probe Types	3
3	(a) Bearing Inspection Assembly. (b) Close-up of Inner Bearing Race and Magnetic Perturbation Probe	5
4	Magnetic Signals Obtained from Typical Bearing Races	6
5	Sketch Showing Scan Track Limits	10
6	Photomicrographs of Selected Specimens	11
7	Photomicrograph Showing Raceway Deterioration During Endurance Testing	13
8	Inspection Records with Typical Signals (Prior to Endurance Testing)	15
9	Inspection Records with Typical Signals (Prior to Endurance Testing)	16
10	Selected Records with Expanded Time Base	18
11	Inspection Records with Typical Signals (Subsequent to Endurance Testing)	19
12	Inspection Records with Typical Signals (Subsequent to Endurance Testing)	20
13	(a) Scribe Lines. (b) Signals Caused by Defect (D) and Reference Scribe Lines (SL)	26
14	Specimen #3 Defect Signal at 5° and Corresponding Defect	28

LIST OF FIGURES (Cont'd)

<u>Figure</u>	<u>Title</u>	<u>Page</u>
15	Specimen #6 Defect Signal at 5° and Corresponding Defect	29
16	Specimen #23 Defect Signal at 312° and Corresponding Defect	30
17	Specimen #25 Defect Signal at 195° and Corresponding Defect	31
18	Specimen #69 Defect Signal at 50° (a) and (b), Corresponding Defect (e), and Etched Subsurface Plastic Zone (d)	32
19	Same Defect (Specimen #69 at 50°) Shown in Figure 18, but 0.001 cm (0.0004 inch) Deeper	33
20	Specimen #74 Defect Signal at 226° and Corresponding Defect; (b) and (d) Show the Expanded Signal Before and After Endurance Testing, Respectively	34
21	Specimen #85 Defect Signal at 305° and Corresponding Defect	35
22	(a) Schematic View of Magnetic Perturbation Signal having Peak Separation ΔP Caused by Defect at Depth D, (b) Plot of ΔP Versus D for Several Defects	36
23	Spalls (a-b) and Pre-Spall Cracking (c-d) at Surface Indents	39
24	Section Through Crack at Trailing Edge of Indent (a) Unetched, (b) Etched	40
25	Subsurface Crack Configuration	41
26	Butterfly Formed at Inclusion, (a) Etched (b) Unetched	42

LIST OF FIGURES (Cont'd)

<u>Figure</u>	<u>Title</u>	<u>Page</u>
27	Section Through Bearing #74 Showing Plastic Zone Shift of 2° from Centerline of Bearing	44
28	Schematic Showing Defect Locations and Sub-surface Plastic Zone	50
29	Life Prediction - Failure Initiated at Subsurface Inclusion	52
30	Spall at Predicted Site in Bearing #130	53
31	Planar Duplex Inclusion, Showing Silicate or Aluminate "Backbone" with Sulfide Sheet	55

I. INTRODUCTION

Studies of boundary layer flows have been made for two reasons; one is the practical need for boundary layer solutions in design problems; the other is the desire to achieve a better theoretical understanding of the mechanism of boundary layer flows. The calculation method described herein was designed to expedite both of these objectives. It makes recent advances in the state of the art available in the form of a convenient tool for those who are interested in ends rather than means. For those concerned with theoretical investigations of boundary layer flows, it overcomes the technical problems of solving the equations of motion and thereby emphasizes the physical assumptions necessary to circumvent our ignorance and inability to describe basic turbulent transport processes. A variety of assumptions can, therefore, be tested free from approximations related to the solution of the equations. Although a specific turbulent effective viscosity hypothesis is included in the program for practical calculations, it is wholly contained in a subroutine. The subroutine may easily be replaced by an alternative form.

The present report is an extension of Reference [1] to compressible flow. Also described are significant improvements and simplifications of the numerical method which apply to both incompressible and compressible versions of the program.

The compressible version of the program includes solution of the thermal energy equation and allows for necessary fluid property variations. Comparison of compressible flow data and heat transfer data may be found in Reference [2]. Somewhat more involved extensions of this program have also been used to investigate more complicated models which calculate mean turbulent energy fields and, at the Stanford Conference on Computation of Turbulent Boundary Layers [3], have been compared with calculations using the more simple effective viscosity hypothesis. This simple hypothesis performs remarkably well in predicting data and this has now been well documented in the literature [4,5,6]. Therefore, it is possible to concentrate on computational details in this report. Also, of course, the program can be operated entirely in a laminar mode where the problem is purely numerical.

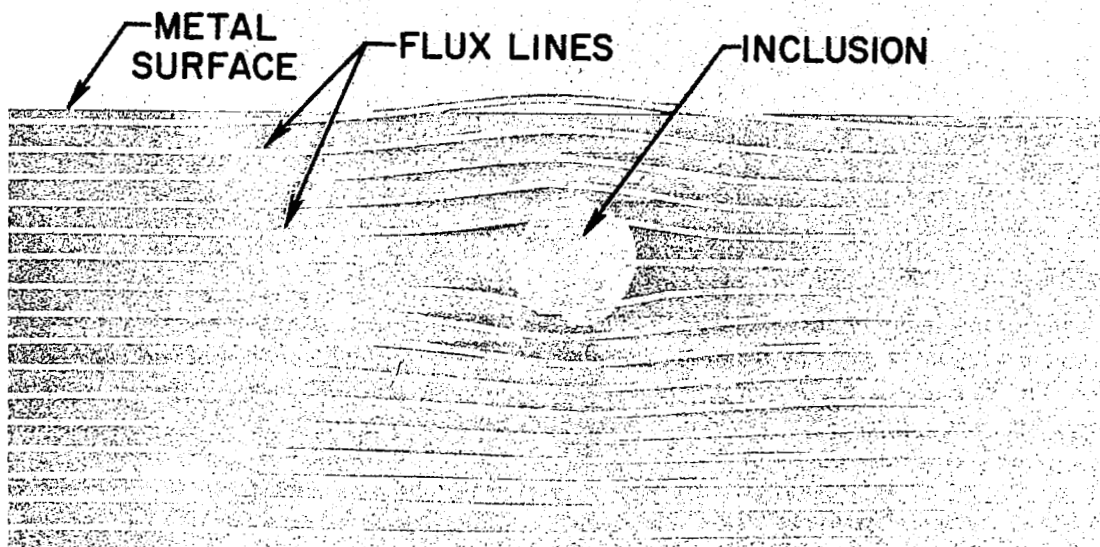
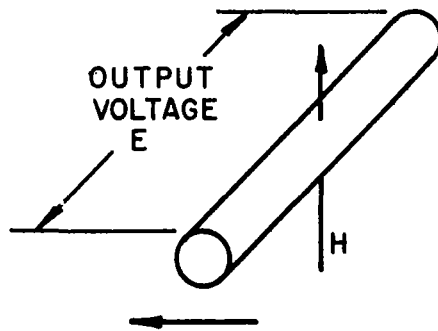


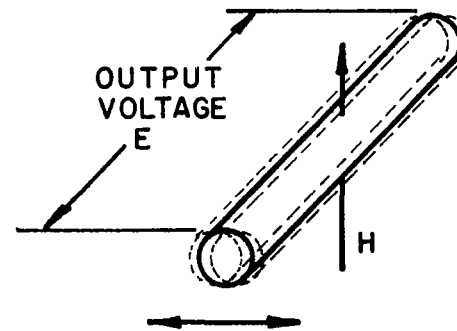
FIGURE 1. PERTURBATIONS IN MAGNETIC FLUX CAUSED BY INCLUSION IN FERROMAGNETIC MATERIAL



VELOCITY (v_f) OF FIELD (H)
RELATIVE TO STATIONARY CONDUCTOR

$$E = C_1 H v_f$$

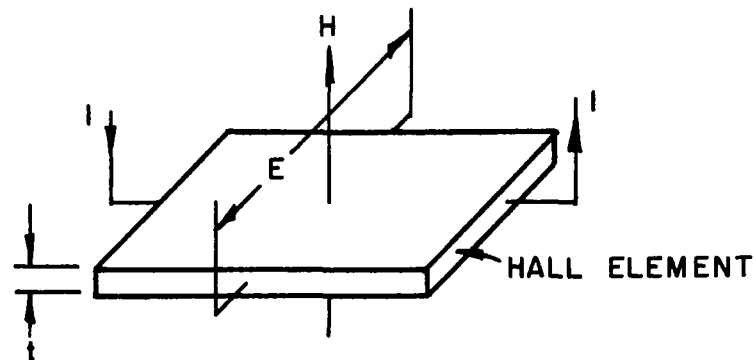
TYPE 1



MAGNETIC FIELD (H) STATIONARY,
CONDUCTOR VIBRATED AT HIGH FREQUENCY

$$E = C_2 H v_c$$

TYPE 2



$$E = \frac{R}{t} I H$$

TYPE 3

PROBE TYPES

FIGURE 2. FLUX SENSITIVE PROBE TYPES

is vibrated by a piezoelectric transducer, and the change in flux linkages during a vibrational period provides a voltage. Both the coil and vibration-producing transducer are moved as a unit to scan the surface of the material being inspected. A semiconductor device, the Hall effect element, shown as probe type No. 3, provides still a third method of detecting surface flux perturbations. Static measurements can be made with this type probe.

The apparatus used for magnetic inspection of the inner bearing races on this program is illustrated in Figure 3. On this device the race was rotated and the surface scanned by a stationary probe. Signal output from the probe was displayed on the vertical axis of an oscilloscope and a motion picture camera provided the time base for signal traces printed on Linagraph paper.

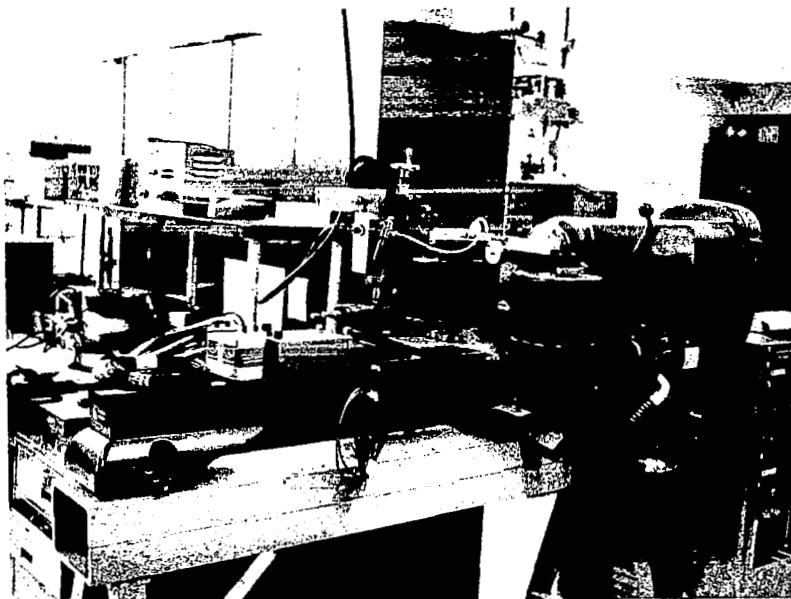
Figure 4 shows typical examples of inspection records obtained on bearing races. In this illustration the individual specimen number and the vertical recording sensitivity are indicated. The upper trace in each case is the magnetic perturbation signal and the lower trace is an angular mark indicator for determining the circumferential angular location of signals occurring on races. Note the outstanding signal from the surface flaw in the record made on specimen Sw 7 and the corresponding photomicrograph of the flaw.

C. Bearing Fatigue Tests

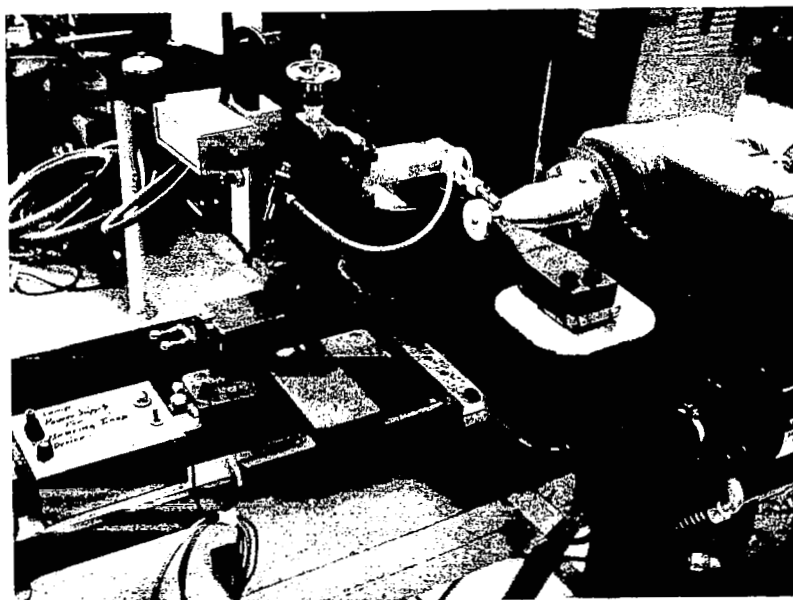
Two groups of 27 bearings each were fatigue tested at 2750 rpm, a radial load of 5800 N (1320 pounds), a maximum Hertz stress at the inner-race-ball contact of 2.42×10^9 N/m² (350,000 psi), with a highly refined naphthenic mineral oil as the lubricant. No external heat was added to the test bearings.

One of the groups (base line test group) of 27 bearings was assembled and fatigue tested immediately after the initial magnetic perturbation inspection of the inner races. The other group of 27 bearings received a brief run-in cycle after assembly but prior to fatigue testing. (The description of this run-in cycle and its effects are the subject of another NASA publication in process.)

The bearings were tested continuously until a fatigue spall occurred on either the inner race, ball, or outer race or until a pre-determined cut-off time was reached. This cut-off time was 4000 hours for the base-line test group and 10,000 hours for the run-in test group.



(a)



(b)

FIGURE 3. (a) BEARING INSPECTION ASSEMBLY. (b) CLOSE-UP OF INNER BEARING RACE AND MAGNETIC PERTURBATION PROBE.

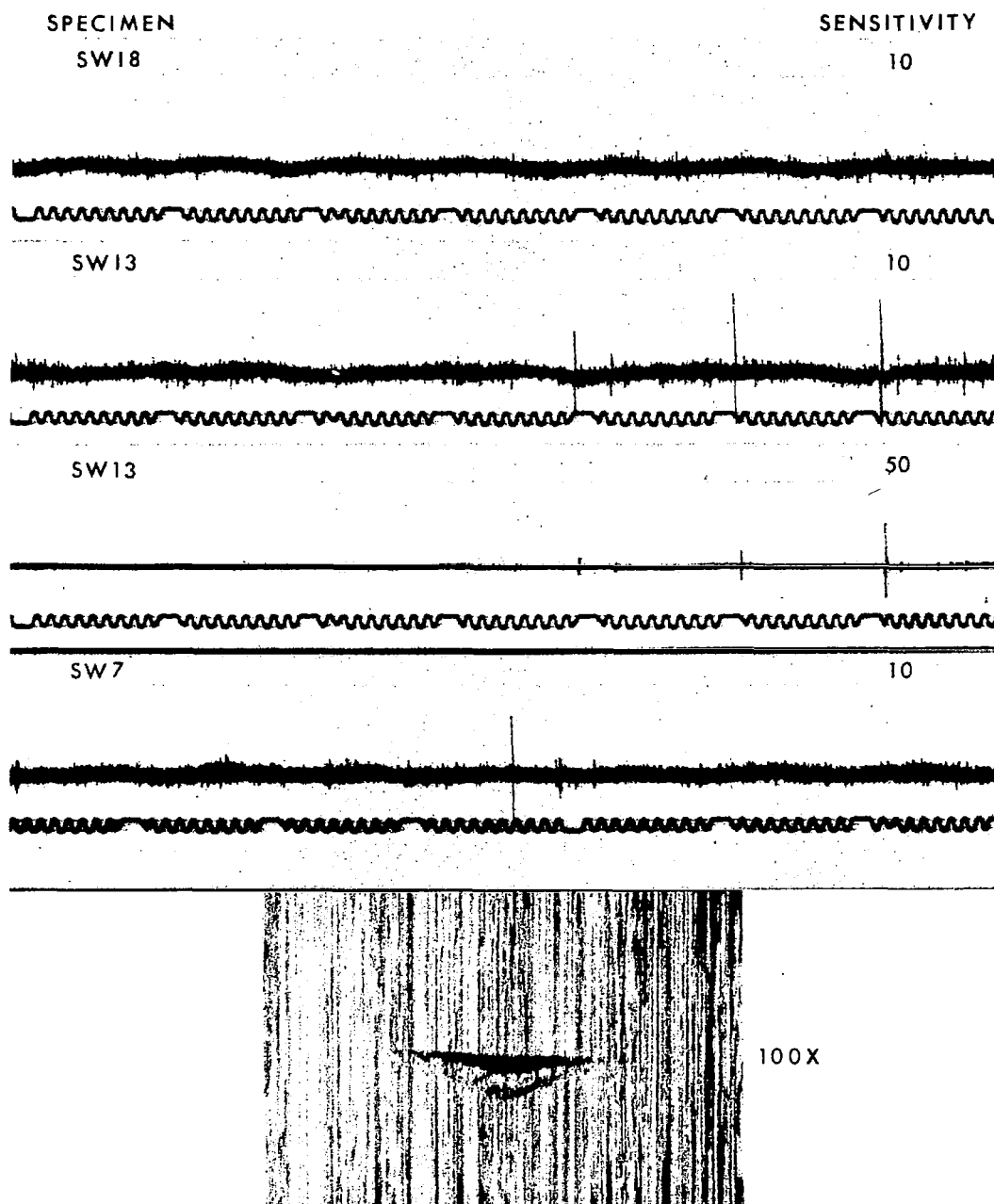


FIGURE 4. MAGNETIC SIGNALS OBTAINED FROM
TYPICAL BEARING RACES

D. Metallurgical Investigation

After endurance tests were complete, approximately 24 bearings were sectioned at selected locations (10 signals; 14 spalls, cracks, indents) for metallurgical examination. Two general sectioning sites were chosen (1) spall locations, and (2) locations corresponding to magnetic perturbation signals, but at which no spall was observed. Sections were studied in both the etched and unetched condition. Details of the sectioning procedure are outlined in Section II. D. 2.

II. DATA SUMMARY AND ANALYSIS

A. Test Bearings

The inner races investigated in this program were taken from 207-size deep-groove ball bearings of the following nominal specifications:

ABEC grade	5
Track diameter, cm (in)	
Inner race	4.2286 (1.6648)
Outer race	6.4544 (2.5411)
Number of balls	9
Ball diameter, cm (in)	1.111 (0.4375)
Conformity, percent	
Inner race	51
Outer race	52

The inner races were from one heat of air-melted, vacuum degassed AISI 52100 steel. Rockwell C hardness of the inner races was 62.0 to 62.5. The balls were AFBMA Grade 10, made from another single heat of AISI 52100 and hardened to Rockwell C 63.5 to 64.0.

B. Inspections

1. Inspection Prior to Endurance Testing

All races were initially inspected under a stereo microscope at approximately 30X magnification. Gloves were used to handle all specimens, and great care was exercised to insure that all specimens were maintained in a good condition. However, in a few instances, local spots which appeared to be "rust" possibly from fingerprints were observed immediately after the initial cleaning. The surfaces of most specimens were free of any apparent surface flaws with the exception of a few very superficial scratches.

Magnetic perturbation inspection records were obtained on all specimens. On each specimen a total of ten adjacent inspection tracks approximately 0.064 cm (0.025 inch) wide with a slight overlap on adjacent tracks were made. The center of the scan region was coincident with the center line of the bearing and inspection traces were centered at 2.5° , 357.5° , 7.7° , 352.2° , 13.0° , 347.0° , 18.2° , 341.7° , 23.5° , and 336.5° . A sketch illustrating the relationship between probe location and scan region limits is shown in Figure 5. The 0° circumferential angle marker, which consisted of a fine scribe line through the hardness impression on the face of the race, is shown, as well as the rotation direction of the race during taking data. This illustration should be referred to in the analysis of the magnetic perturbation inspection records.

Data were recorded by displaying the signal on an oscilloscope and recording the resulting presentation on 35 mm Linagraph paper. A circumferential angular location marker was also recorded on each Linagraph record, and provides a method of determining the location of specific signals on specimens.

After visual analysis of the Linagraph records, specific regions on a number of specimens were re-inspected, magnetically, and expanded sweep Polaroid photographs of signals were obtained. These expanded sweep records permit a more detailed evaluation of the signal source. In addition, photomicrographs of the race surface at approximately 50X magnification were obtained at the location of the signals on most of these specimens.

The visual examination of the bearing races and the associated high magnification photographs disclosed only a few cases in which the void polarity signal could be ascribed to a surface inclusion. Specimen No. 6 shows an extremely small surface flaw that could possibly be the signal source at 312° circumferentially and 347° axially. The only other specimens for which photomicrographs showed surface flaws were specimen Nos. 48, 85, 110, and 129. Figure 6 shows the photomicrographs from these four specimens, and the arrow indicates the surface flaw which was apparently the source of the signal on the magnetic inspection records.

2. Inspection Subsequent to Endurance Testing

All races were re-inspected optically at 30X magnification. It was noted that for both sets of bearings, the endurance testing had the effect of obliterating all pre-existing polishing marks

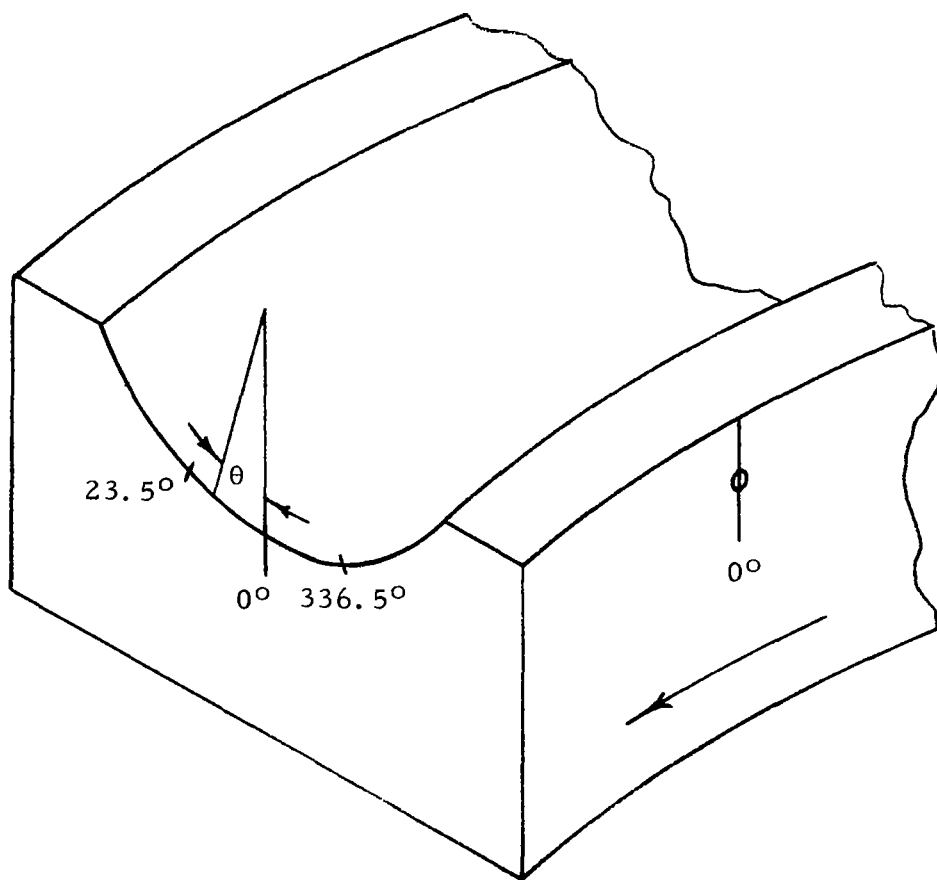


FIGURE 5. SKETCH SHOWING SCAN TRACK LIMITS

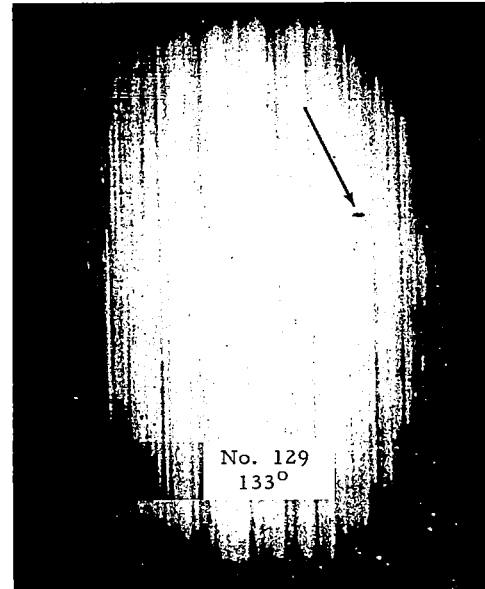
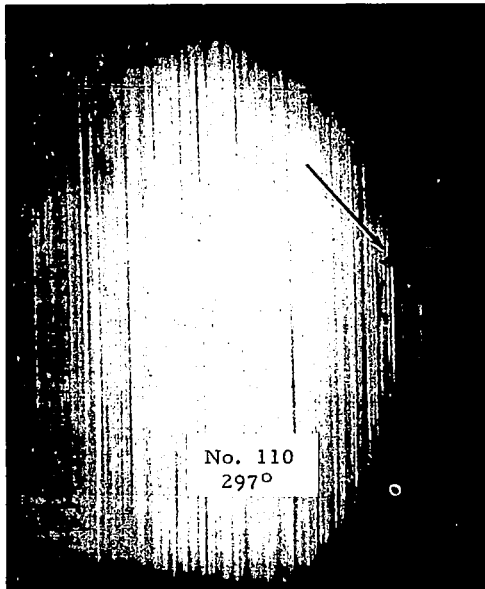
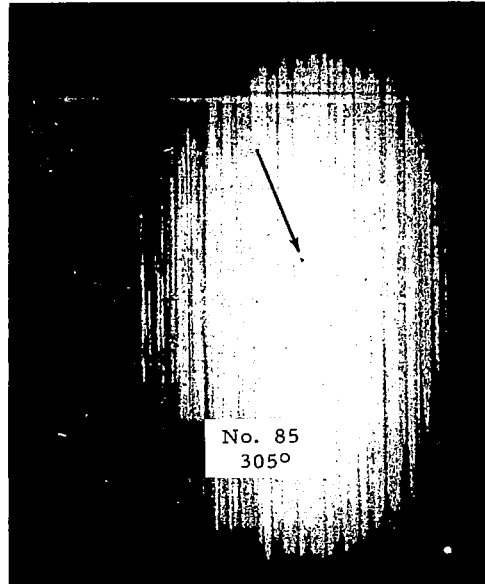
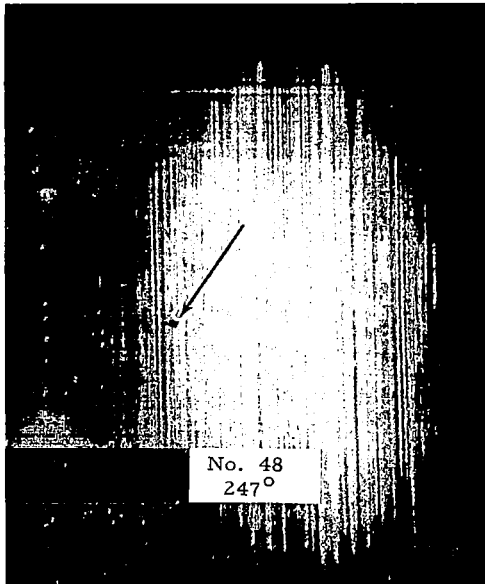


FIGURE 6. PHOTOMICROGRAPHS OF SELECTED SPECIMENS

within the region of ball travel, as shown in Figure 7. The resulting surface was dull and pebbly in texture.

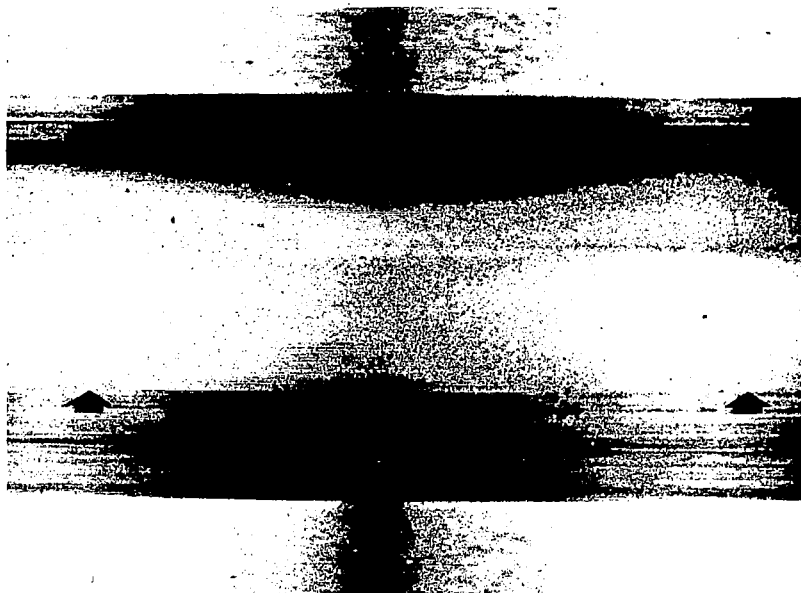
It was further observed that the total width of this "apparent" rolling track was inconsistent from one specimen to another, varying from 42° to 60° among the approximately 20 bearings for which this feature was measured. Shifts in the track centerline ranged up to 14° , averaging 5° from the geometric centerline of the raceway. If this apparent shift in track center was actually caused by a shift in the running track of the ball complement it could be attributed to a thrust component. Such a departure from radial loading would be expected to alter significantly the Hertzian stress distribution within the inner race. Shift data are tabulated, in Table I, for 19 bearings.

Magnetic perturbation inspections were accomplished in a manner similar to those obtained prior to endurance testing, except when severe spalling of a raceway might have damaged a probe. Again, both Linagraph and expanded Polaroid photographic records were taken, and the surfaces were examined at 50X and 100X magnification for signs of cracking at signal locations.

C. Records and Data Tabulation

1. Initial Inspection Records

Selected inspection records from several specimens which showed an "inclusion type" signal are shown in Figures 8 and 9. In each instance, the signal of interest has been indicated by an arrow. The specimen serial number and the location of the track across the specimen groove is also shown. For example, the first trace (Figure 8(a)) is from specimen No. 3 with the track centered at 2.5° . The flaw signal at the arrow is located at approximately 5° circumferentially as determined by referring to the circumferential angular marker. This is the general type of signal obtained from an inclusion; namely, the signal when examined from 0° toward the 360° location first goes downward and then upward, and this "polarity" is typical of inclusion signals and/or voids. Such signals will be called "void polarity." On other specimens rather pronounced signals which have a polarity opposite to an inclusion signal have been observed; these will be called opposite polarity. An excellent example of the latter is shown on the record from specimen No. 116 at the 55° circumferential location (Figure 8(c)).



ball
groove

FIGURE 7. PHOTOMICROGRAPH SHOWING RACEWAY DETERIORATION DURING ENDURANCE TESTING (Arrows indicate extreme limits of surface damage)

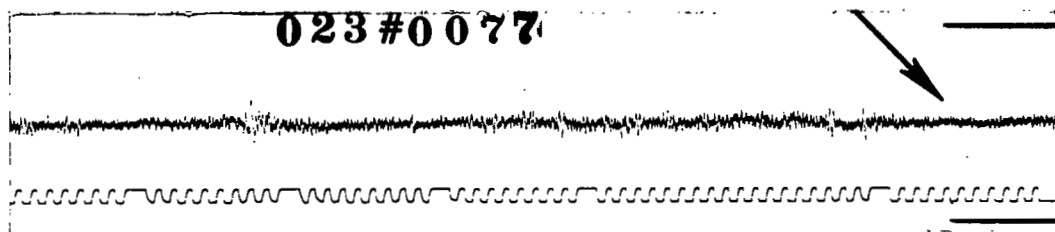
TABLE I
ROLLING TRACK SHIFTS AND WIDTHS

<u>Bearing Number</u>	<u>Apparent Track Width (°)</u>	<u>Apparent Centerline Shift (°)</u>
3	48	-0.5
6	57	0.0
7	49	3.0
23	50	1.0
24	47	2.0
25	51	5.0
48	46	-1.0
69	56	1.0
74	60	14.0
85	49	2.5
94	53	7.0
110	48	3.0
116	45	1.5
120	48	10.0
129	47	5.0
130	49	4.5
137	48	10.0
146	45	-1.5
160	42	4.0

Average Width: 49°
Average Shift: 3.8°



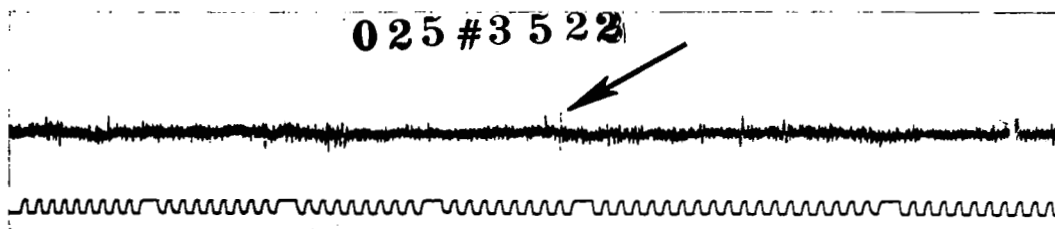
(a)



(b)



(c)



(d)

FIGURE 8. INSPECTION RECORDS WITH TYPICAL SIGNALS (PRIOR TO ENDURANCE TESTING). SIGNAL IN (c) IS OF OPPOSITE POLARITY.

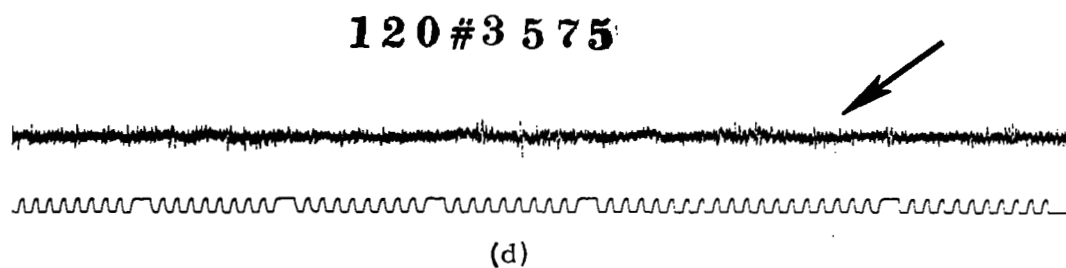
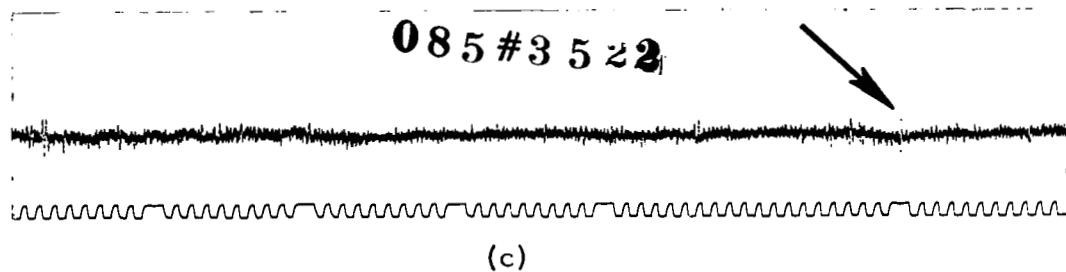
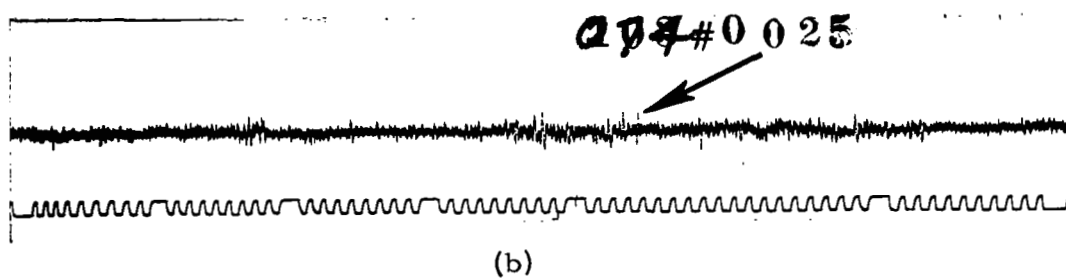
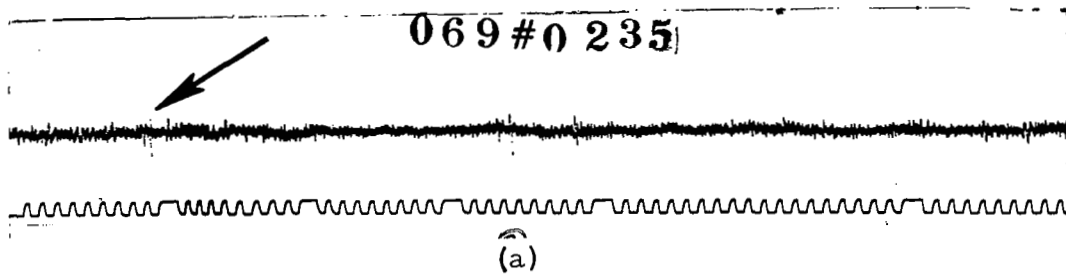


FIGURE 9. INSPECTION RECORDS WITH TYPICAL SIGNALS (PRIOR TO ENDURANCE TESTING)

Several records with expanded "sweeps" or horizontal time base expansions are shown in Figure 10. These records show characteristics such as peak separation and local signal to background.

2. Post-Endurance Testing Records

A number of inspection records taken following endurance testing of 54 bearings are shown in Figures 11 and 12. Where applicable, the signal corresponding to an earlier, pre-endurance test signal has been marked with an arrow; these data should be compared with Figures 8 and 9, showing the pre-run data. It is interesting to notice that the average background signal amplitude appears to have increased significantly, frequently making it difficult to locate an initially highly visible signal. Actually, it will be seen later that most of the defect signal amplitudes have changed little. The background has remained essentially constant, although in a few instances may have increased slightly. It should be pointed out that in estimating signal amplitudes in millivolts, the Polaroid expanded records are employed, and the precise probe positioning is adjusted by hand for maximum signal resolution. This procedure helps in bringing the signal out of the background, as shown in Figure 10. The apparent background increase can be attributed to the fact that a probe differing in sensitivity from that employed for the pre-endurance run data was used in recording the later Linagraph data; a probe identical to the earlier one was used in taking expanded signal data. By utilizing recognizable background features, it is possible to pick out defect signals, and to establish the precise location of the defect relative to the bearing race. This aspect of the work will be discussed further in Section II. D. 2.

3. Tabulation of Data

After examining the pre-endurance run inspection records from all specimens, data were catalogued on the locations of all void polarity signals and a limited number of opposite polarity signals. The data thus catalogued include the following:

- (a) Specimen serial number
- (b) Circumferential and axial location of specific signals

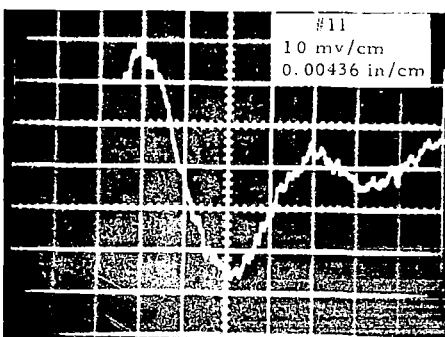
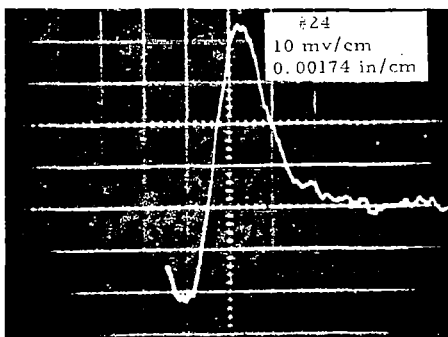
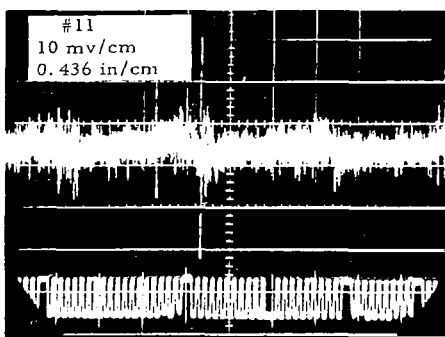
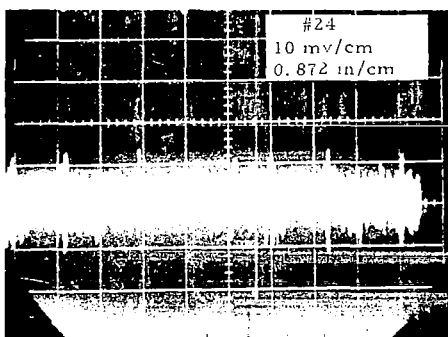
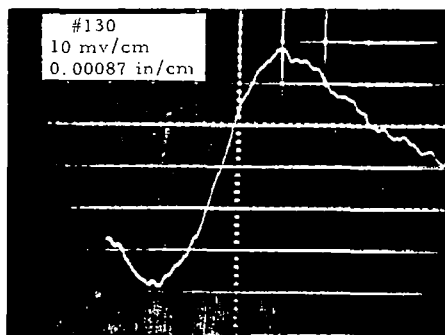
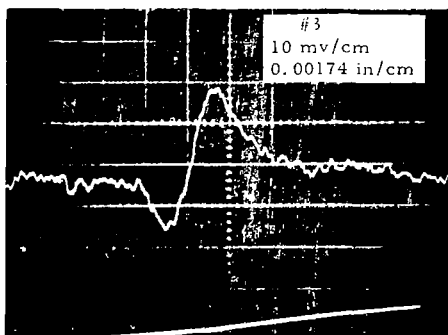
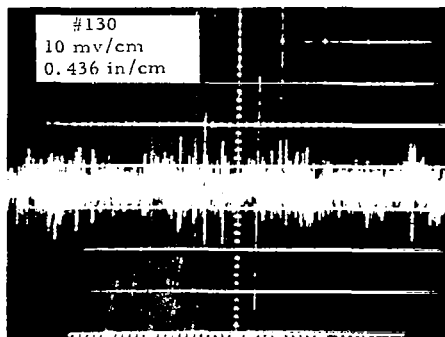
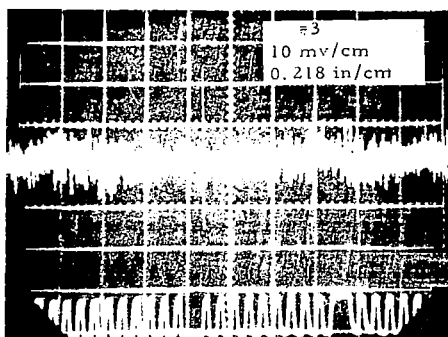


FIGURE 10. SELECTED RECORDS WITH EXPANDED TIME BASE

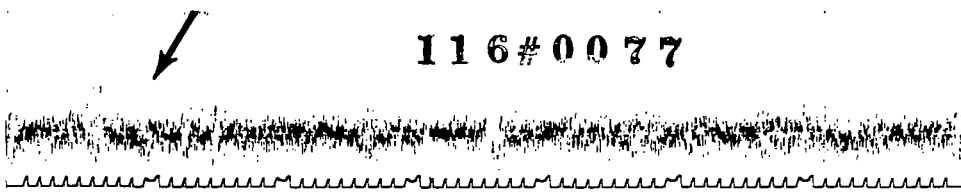
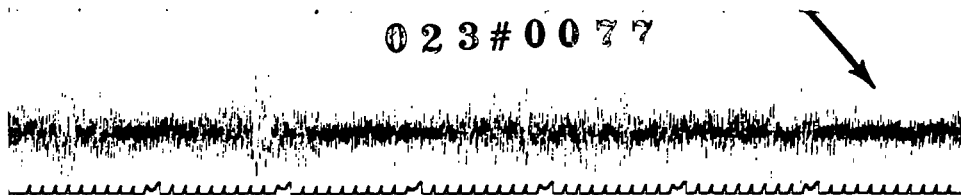
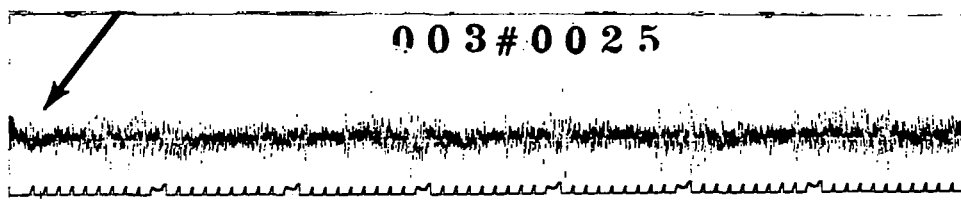


FIGURE 11. INSPECTION RECORDS WITH TYPICAL SIGNALS (SUBSEQUENT TO ENDURANCE TESTING). SIGNAL IN (c) IS OF OPPOSITE POLARITY.

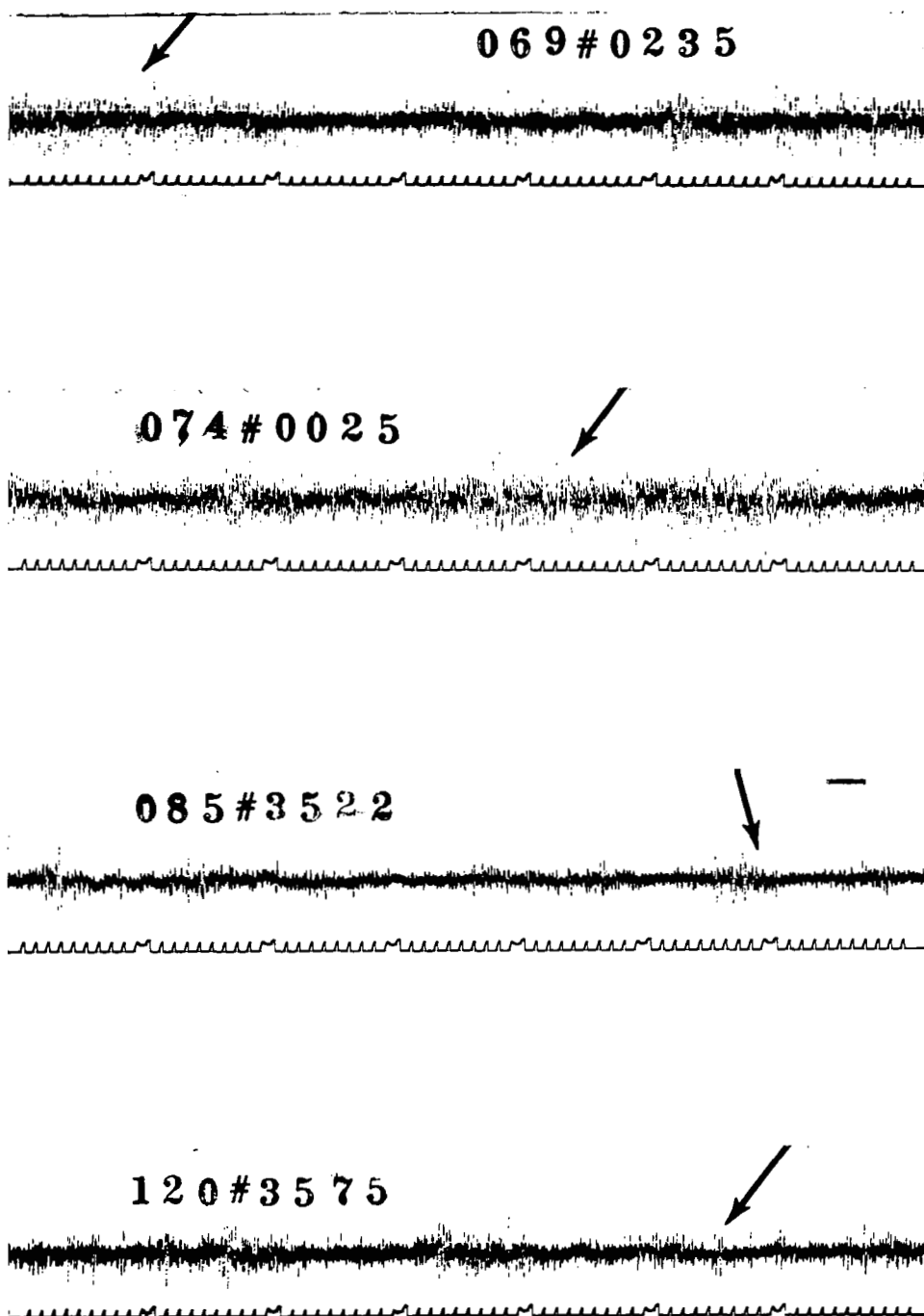


FIGURE 12. INSPECTION RECORDS WITH TYPICAL SIGNALS (SUBSEQUENT TO ENDURANCE TESTING)

- (c) Signal amplitude and polarity obtained on both the Linagraph and from the expanded Polaroid records
- (d) Peak separation of the signal
- (e) Signal-to-magnetic background ratio
- (f) Result of the visual inspection and the examination of the surface photomicrograph.

These data are concisely presented in Table II.

D. Metallurgical Investigation

1. General

A number of important points were considered during the course of the metallurgical phase of this work. A particularly crucial factor was the effort to establish conclusively the point of origin of all spalls. Further, it was important to check the relationship of void polarity signals with possible subsurface defects at the sites corresponding to the signals. Where failures had occurred at these sites, it was useful to consider in detail the flaw signal characteristics, and to extrapolate its meaning in order to determine the most likely size and depth of the nucleating defect. Where failure had not occurred at a defect site, the questions of size, depth, and possibly local stress-induced plastic zones remained. It was relevant here to consider also the size and extent of the rolling contact induced, subsurface stress transformed zone.

2. Precision Sectioning Technique

Sectioning of the inner bearing races at signal locations was carried out in the following way. The circumferential and radial locations were established using expanded sweep data. Lines (Figure 13a) were then inscribed ± 0.127 cm (± 0.050 inch), measured circumferentially, from the signal location; these were used as "magnetic markers," as shown in Figure 13b. From the magnetic traces, it was possible to calculate the location of the flaw, assuming that the zero crossing of the signals corresponded to the centroids of the defects and to scribe lines. Accuracy using this procedure usually was sufficient to specify defect locations within ± 0.005 cm (± 0.002 inch).

TABLE II

INSPECTION DATA SUMMARY ON 207 mm BORE BEARINGS

Ring No.	Angle (°)		Signal Characteristics						Remarks	Photo	Hours
			Void		Opposite		Peak				
	Circ.	Axial	Amp (mV)		Amp (mV)		Separation				
			Lina.	Polar.	Lina.	Polar.	cmx10 ⁻³ (10 ⁻³ in)				
3	5	3.5	28	39			4.6 (1.8)	3/1	N***	4,000.0	
6	315	341.7	15				--	1.2/1 not signal of interest on expanded record, P	N	10,000.0	
6	312	347.0	40	53			4.6 (1.8)	5/1 local 4/1 ave., P	(speck 0.0127cm)	10,000.0	
6	180	352 18*	--	--		45	--	P		10,000.0	
7	263	2.5	--	20			Unipolarity	2.5/1 possibly angled defect with remainder at 262° and 357.5°		3,077.5	
11	315	352.2 18.2*	--	--	55	55	24.4 (9.6)	6/1, P		10,000.0	
12	55	357.5 13.0*	--	--	40		--				
15	166	352.2 18.2*	--	--	40		--				

* Opposite polarity signal and these values show limits over which signal persisted on adjacent scan tracks.

** Void polarity signal probably located in overlap region of adjacent scan tracks.

*** Careful examination of photomicrograph shows nothing.

P Prestressed during run-in cycles.

TABLE II (Cont'd)

Ring No.	Signal Characteristics										Remarks	Photo	Hours
	Angle (°)		Void		Opposite		Peak						
	Circ.	Axial	Amp (mV)	Amp (mV)	Amp (mV)	Amp (mV)	Separation	Separation					
			Lina.	Polar.	Lina.	Polar.		cmx10 ⁻³ (10 ⁻³ in)					
23	327	7.7	22	22				4.6 (1.8)	4/1 local 2/1 ave., P		--	10,000.0	
24	9	7.7	52	67				5.6 (2.2)	6/1 local 5/1 ave.	N		1,902.7	
25	195	352.2	25	30				7.1 (2.8)	2.5/1, P	N		9,940.4	
46	310	357.5 23.5	--	--	35			--					
48	250	18.2	30	60				6.1 (2.4)			0.0025x0.005cm surface incl.	1,826.0	
66	72	18.2	21	--				--	expanded record did not show signal of interest				
69	50	23.5	33	38				5.3 (2.1)	4/1 local 4/1 ave., P	N		10,000.0	
74	226	2.5	20	25				7.8 (2.8)	2/1 local 1.5/1 ave.	N		4,000.0	
82	224	357.5 2.5*	19	36				4.8 (1.9)	3/1 local on Polaroid P	N		10,000.0	
85	305	347 352*	27	49				6.1 (2.4)	7/1 local on Polaroid @ 351° 5/1 ave. on Polaroid		0.0025cm and 0.004x0.005cm	4,000.0	

TABLE II (Cont'd)

Ring No.	Angle (°)		Void Amp (mV)		Signal Characteristics Opposite Amp (mV)		Peak Separation	Remarks	Photo	Hours
	Circ.	Axial	Lina.	Polar.	Lina.	Polar.	cmx10 ⁻³ (10 ⁻³ in)			
89	130	357.5	20	22			14.5 (5.7)	2/1 very broad, prob- ably inclusion perhaps 0.012cm deep, P	N	10,000.0
96	200	18.2	20	20			7.8 (2.8)	1.5/1	N	
110	297	347	20	29			5.0 (2.0)	3/1	0.0025x0.005cm surface incl.	3,635.0
115	90	352.2 23.5*			35		--			
116	55	2.5 18.2*			30		--	4/1		1,969.4
120	288	357.5 and also some 352.2	25	47			5.0 (2.0)	3/1 local, P	N	10,000.0
129	133	2.5	20	25			6.1 (2.4)	2/1 local	0.0025x0.0075cm	4,000.0
	132	357.5**	20	--				no expanded	surface incl.	
130	308	357.5 2.5**	25 42	58			6.6 (2.6)	6/1 at 1°	N	1,333.3
132	19	13.0	25				--	no expanded record		

TABLE II (Cont'd)

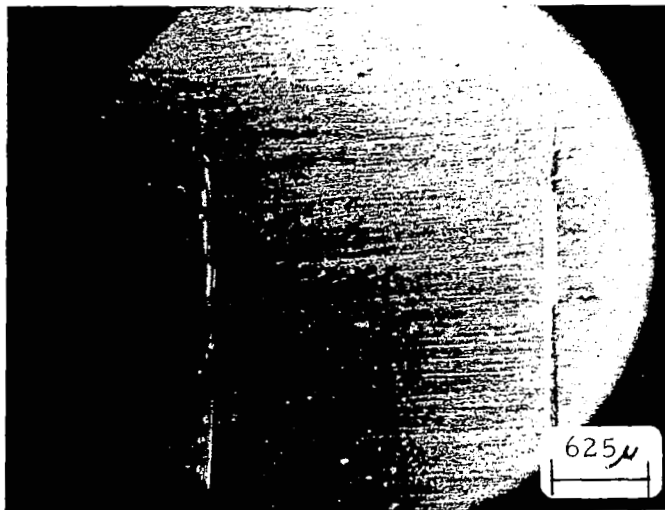
Ring No.	Signal Characteristics										Remarks	Photo	Hours
	Angle(°)		Void		Opposite		Peak		Separation cmx10 ⁻³ (10 ⁻³ in)				
			Amp (mV)		Amp (mV)								
	Circ.	Axial	Lina.	Polar.	Lina.	Polar.	Lina.	Polar.					
136	358	352.2 13.0*	--	--					--				
					40								
148	170	2.5	20	--					--	2/1 no expanded record, P	N		9,655.0
148	233	18.2	40	35					12.7 (5.0)	3/1, P			9,655.0
155	8	352.2 18.2*	--	--					--	P			10,000.0
					40								
160	149	18.2	30	--					--	3/1 no expanded record	N		4,000.0
165	74	2.5	25	--					--	2/1 no expanded record, P			3,126.0
168	287	13.0	25	--					--	2/1 no expanded record, P	N		10,000.0

* Opposite polarity signal and these values show limits over which signal persisted on adjacent scan tracks.

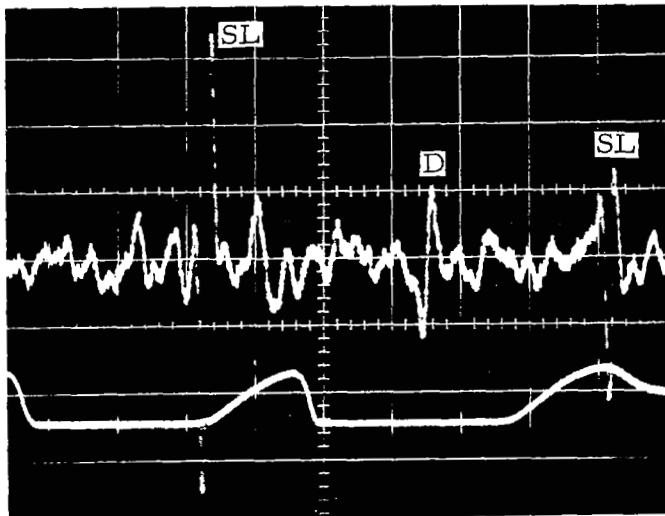
** Void polarity signal probably located in overlap region of adjacent scan tracks.

*** Careful examination of photomicrograph shows nothing.

P Prestressed during run-in cycles.



(a)



(b)

FIGURE 13. (a) SCRIBE LINES. (b) SIGNALS CAUSED BY DEFECT (D) AND REFERENCE SCRIBE LINES (SL)

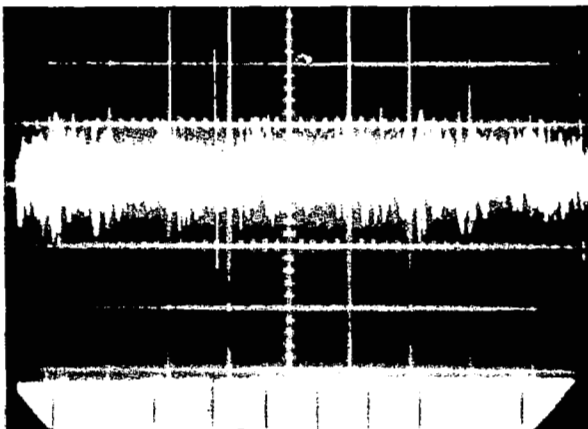
After establishing the apparent defect location, a radial section of the race was removed using a diamond saw. The cut surfaces were then accurately paralleled by milling, and the flaw location precisely determined by referencing a milled face to scribe lines. It was possible, using this scheme, to mill down to the defect region, stopping 0.018 cm (0.007 inch) from the apparent location. Several specimens then could be mounted together for metallographic polishing, and consecutive 0.00063 cm (0.00025 inch) layers were carefully removed. Between each removal, optical microscopy (100X) was utilized in scanning the region just below the raceway surface until the defects were discovered. Once the defect was located, several sections were made to determine the actual inclusion size. Metallographic examination was carried out at 100X and 500X, with the specimens in both the etched (5% nital) and unetched condition. Eight defect void polarity (defect) signal locations were checked using this technique.

Some of the spalled bearing races also were sectioned, both radially and circumferentially. These sections were studied in both the etched and unetched state, and will be discussed briefly later.

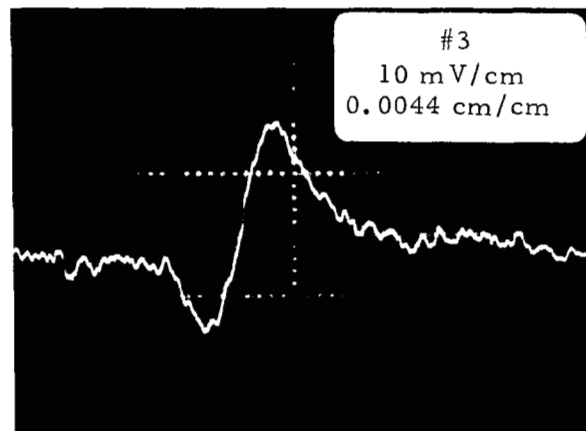
3. Void Polarity Signals

Figures 14 - 21 show a series of compressed and expanded records taken prior to endurance testing, together with photomicrographs of the inclusions located metallographically at the sites corresponding to the signal locations. It should be noted that a non-metallic inclusion was located at all eight of the locations chosen. From these sectioning results, a linear relationship between peak separation ΔP and defect depth D , measured from track surface to defect center, was obtained (Figure 22). Points identified with x were from planar sulfide disks.

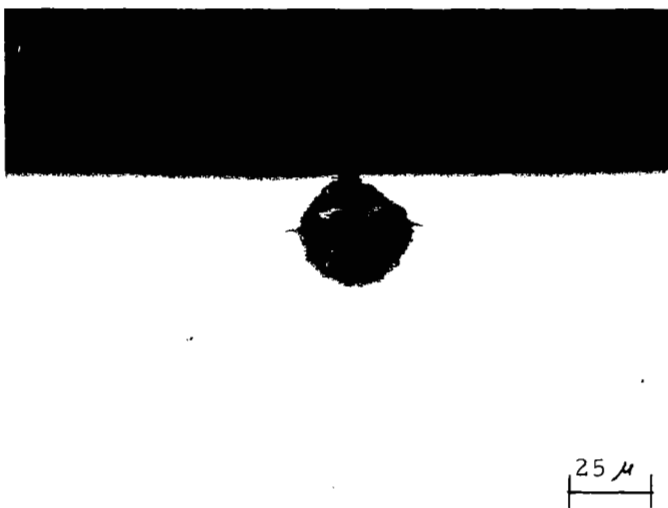
Specific details concerning these inclusions will be expanded upon in the Discussion section. However, several general observations can be made. Two general types of inclusions are present: (1) essentially spherical silicates or aluminates (Figure 14, for example) and (2) planar sulfide disks. Cracks are observed only at the former, and no white etching (plastically deformed) material was observed at any of the sites. The sizes of the particles detected via magnetic field perturbation ranged from 0.0023 cm (0.0009 inch) to 0.007 cm (0.00275 inch); depths were from ≈ 0.0 cm to 0.0075 cm (0.003 inch).



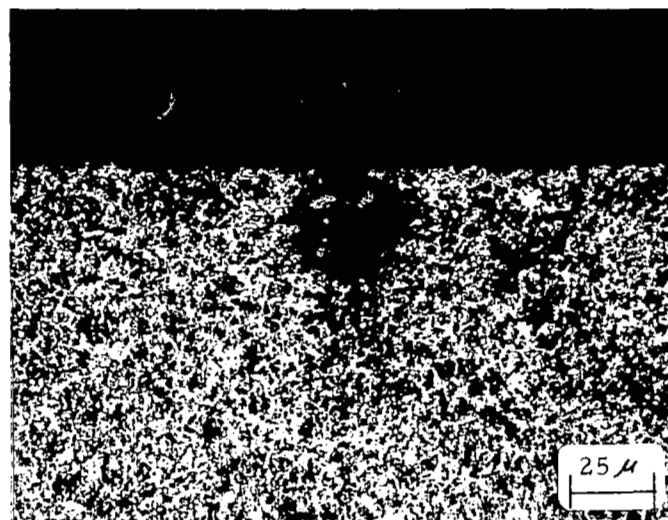
(a)



(b)

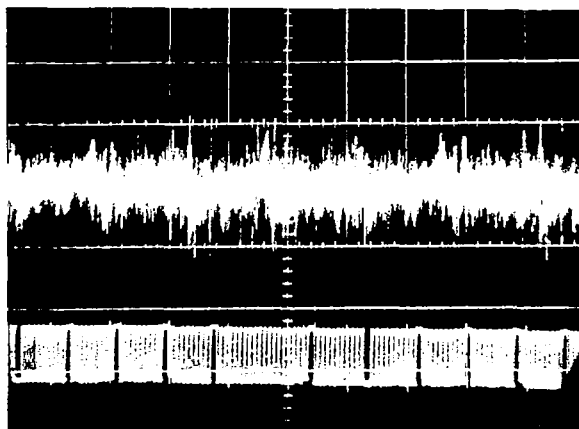


(c)

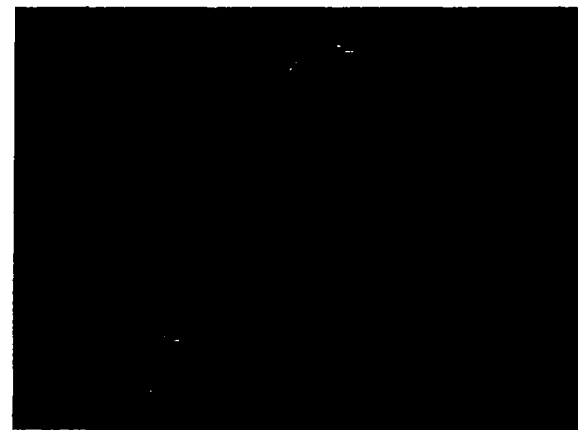


(d)

FIGURE 14. SPECIMEN #3 DEFECT SIGNAL AT 5° AND CORRESPONDING DEFECT. (Note cracking evident in Unetched view (c).



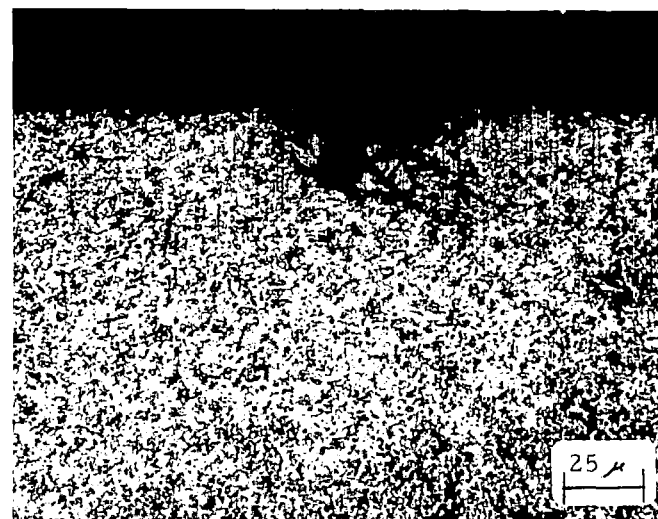
(a)



(b)

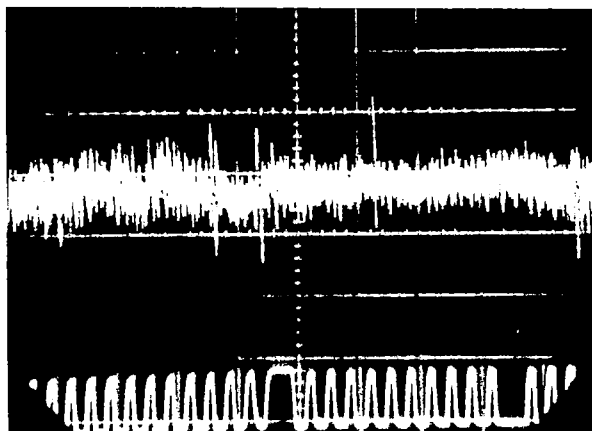


(c)

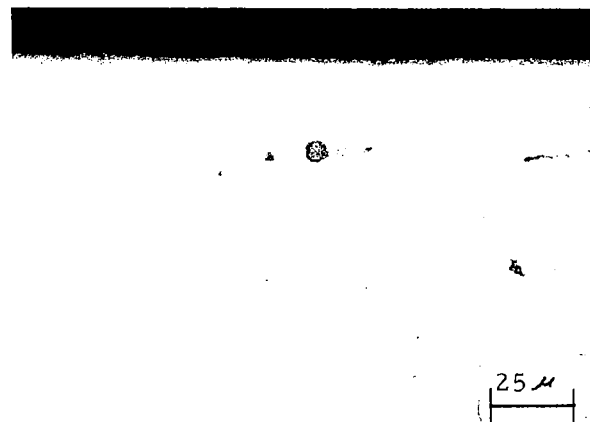


(d)

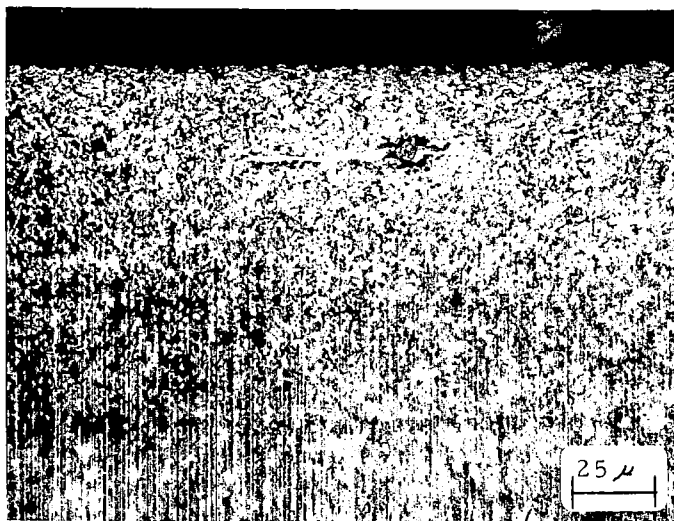
FIGURE 15. SPECIMEN #6 DEFECT SIGNAL AT 312° AND CORRESPONDING DEFECT. (Note cracking evident in unetched view (c)).



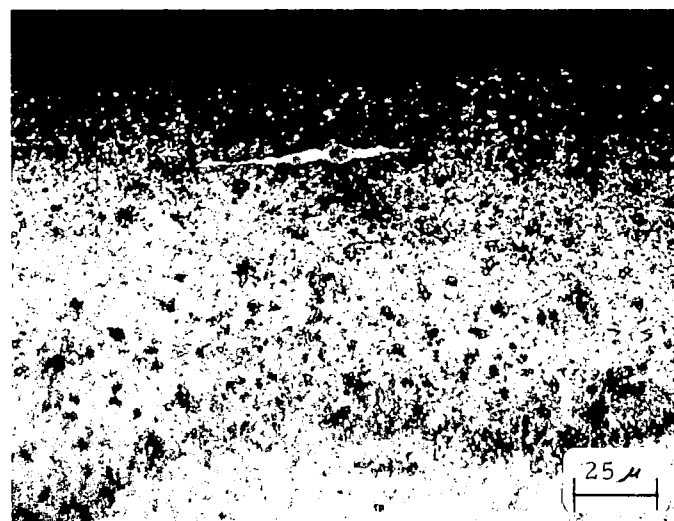
(a)



(b)



(c)



(d)

FIGURE 16. SPECIMEN #23 DEFECT SIGNAL AT 327° AND CORRESPONDING DEFECT.

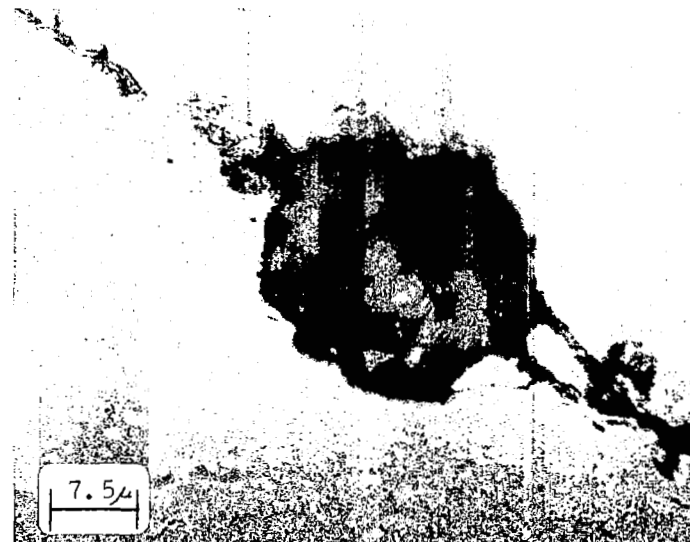
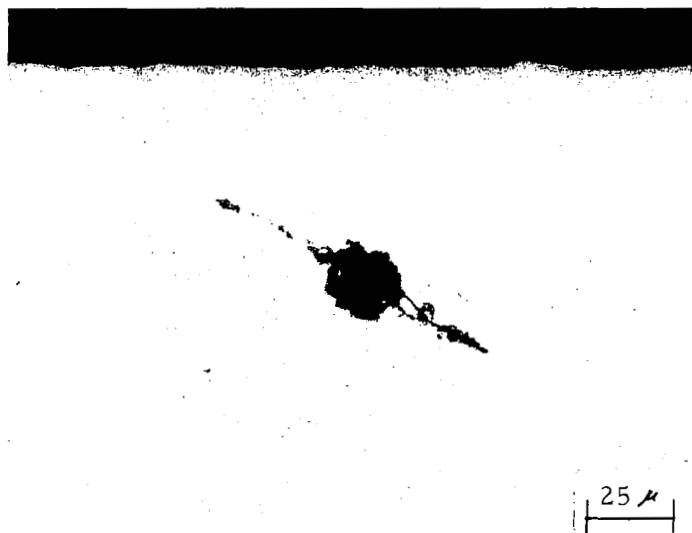
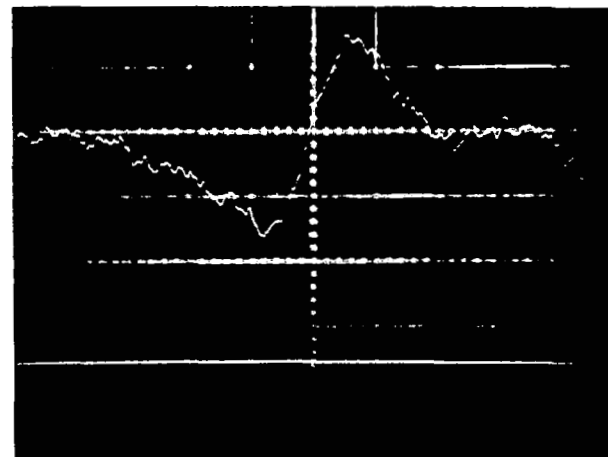
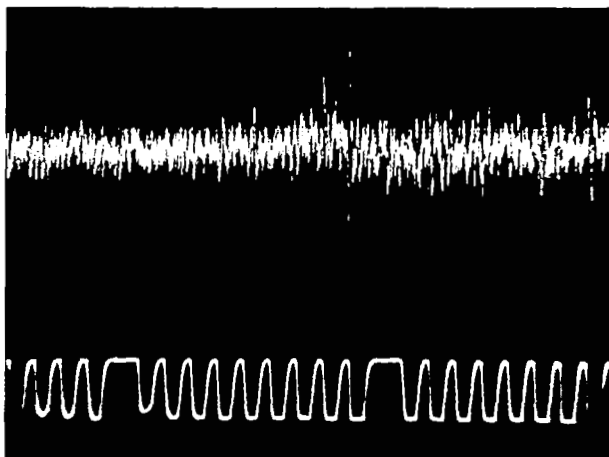
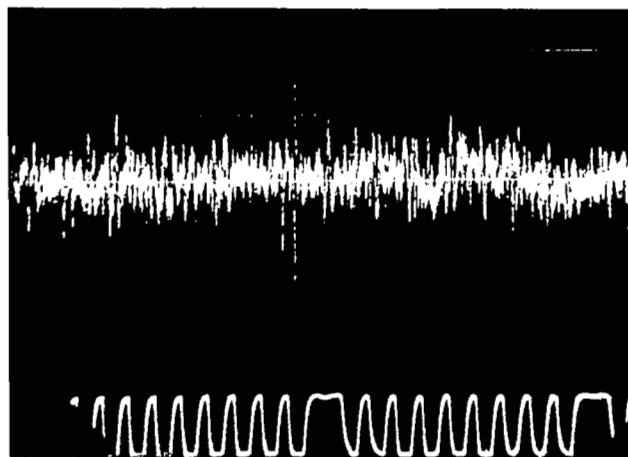
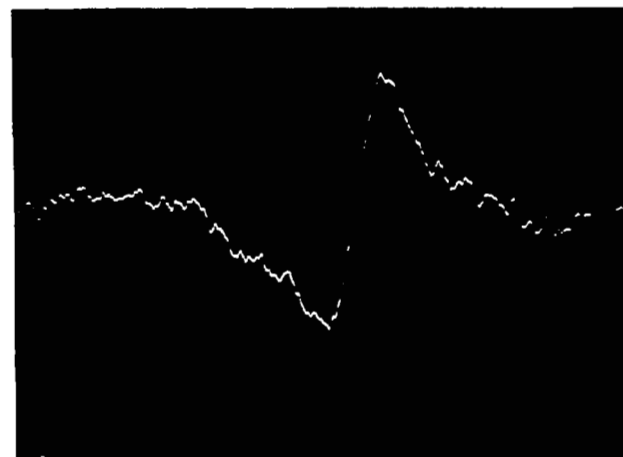


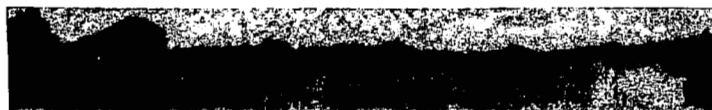
FIGURE 17. SPECIMEN #25 DEFECT SIGNAL AT 195° AND CORRESPONDING DEFECT



(a)

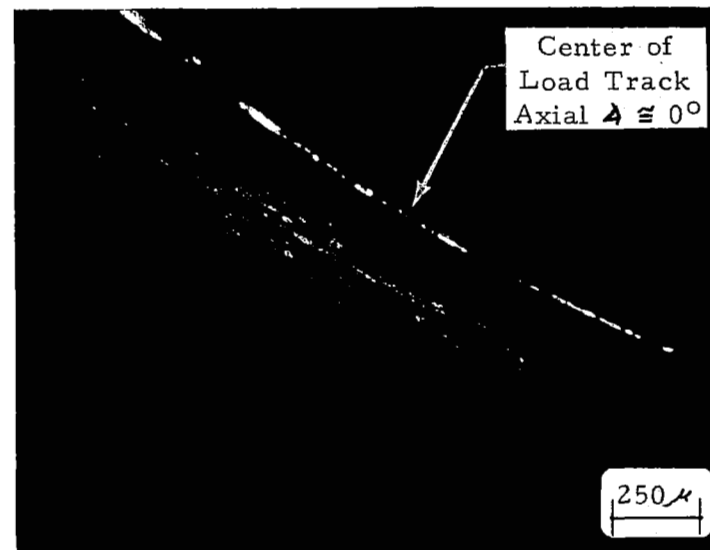


(b)



(c)

25 μ

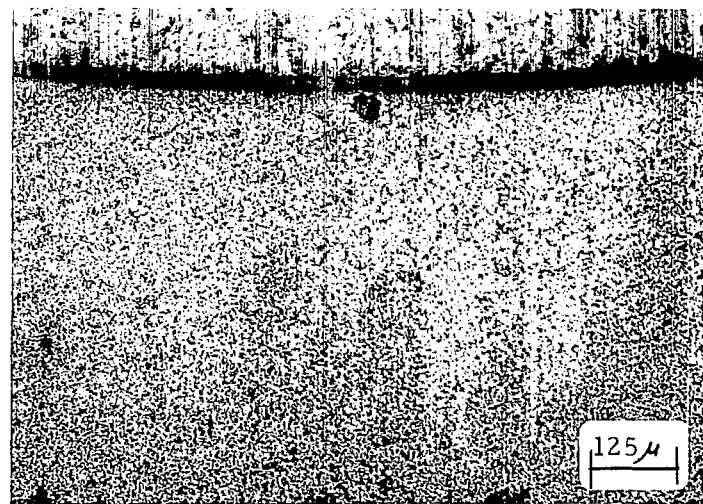


(d)

FIGURE 18. SPECIMEN #69 DEFECT SIGNAL AT 50° (a) AND (b), CORRESPONDING DEFECT (c), AND ETCHED SUBSURFACE PLASTIC ZONE (d).



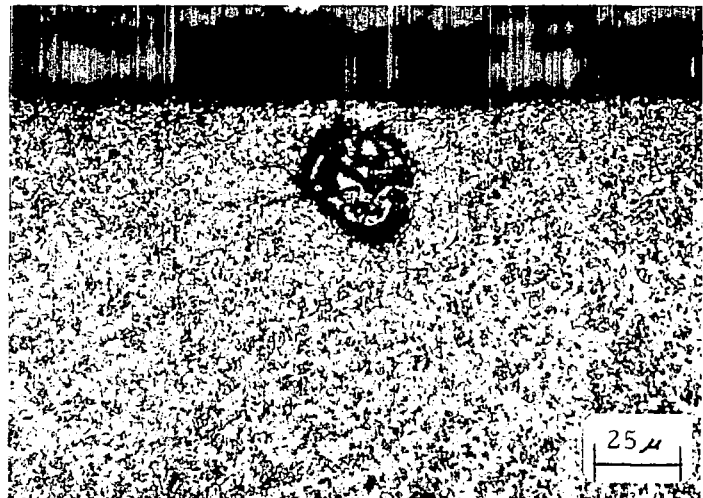
(a)



(b)

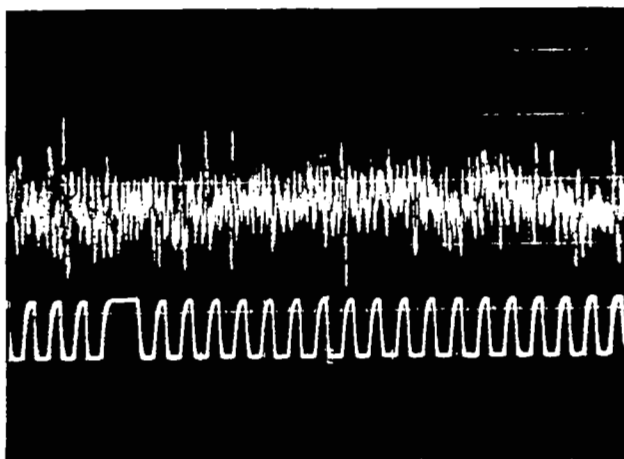


(c)

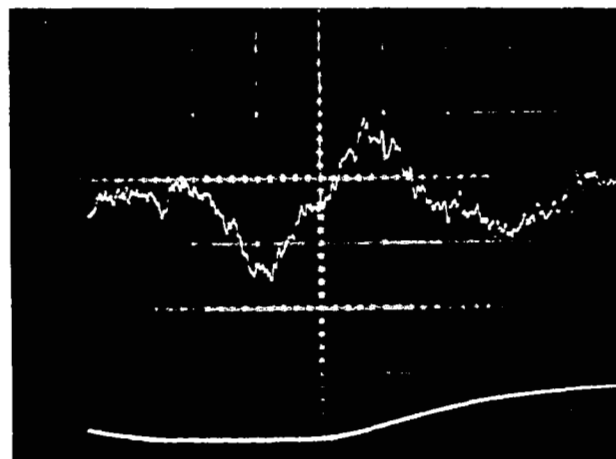


(d)

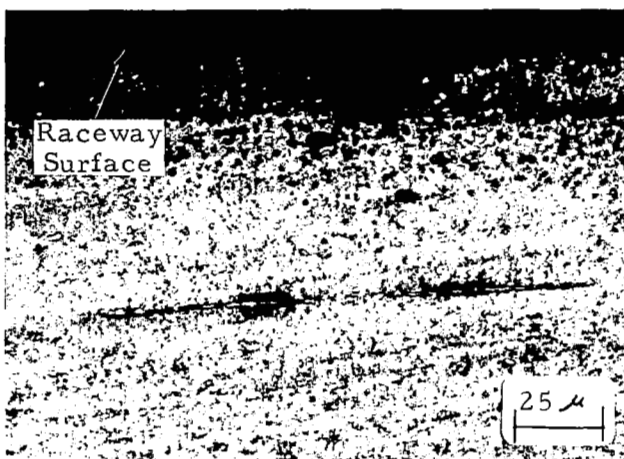
FIGURE 19. SAME DEFECT (SPECIMEN #69 AT 50°) SHOWN IN FIGURE 18, BUT 0.001 cm (0.0004 inch) DEEPER



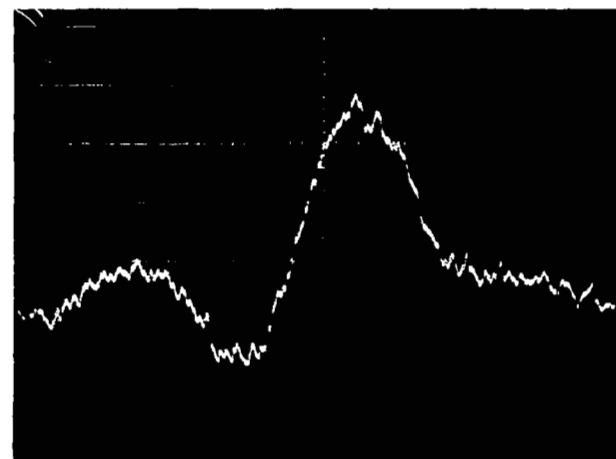
(a)



(b)

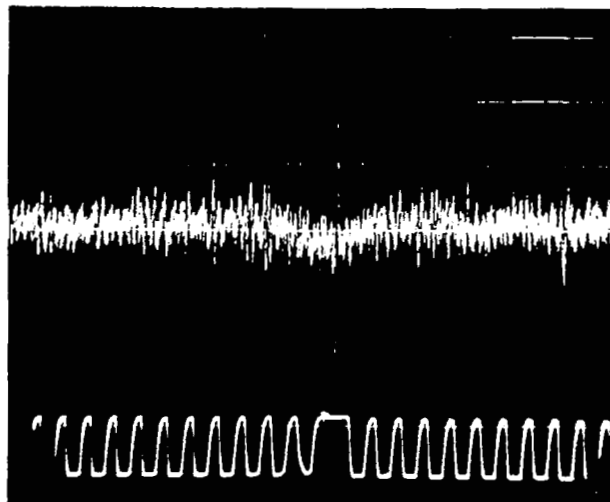


(c)

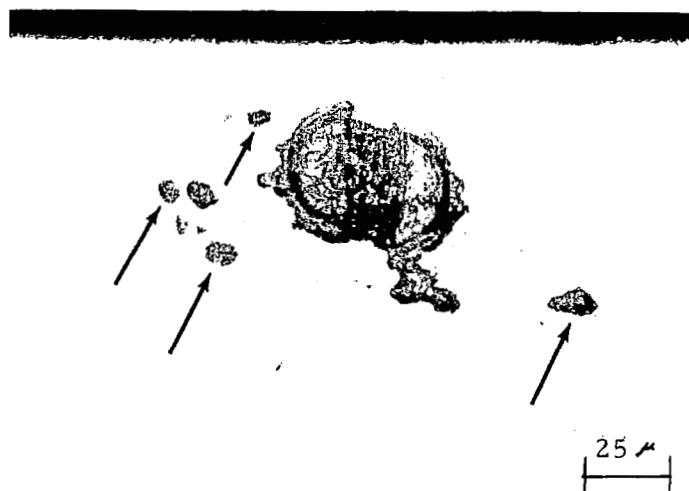


(d)

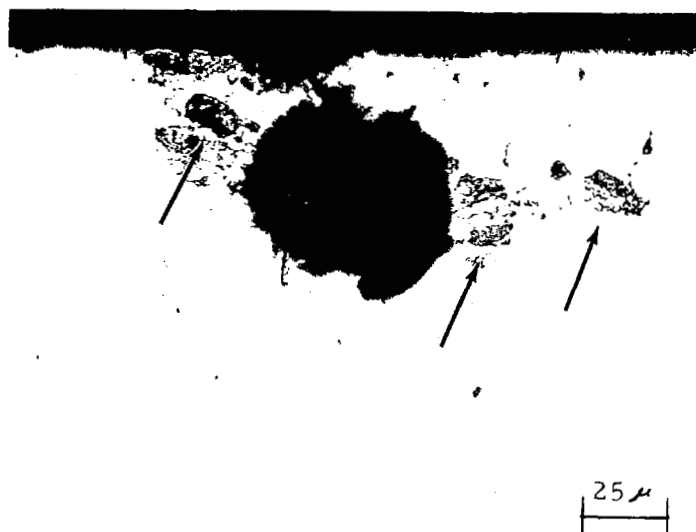
FIGURE 20. SPECIMEN #74 DEFECT SIGNAL AT 226° AND CORRESPONDING DEFECT; (b) AND (d) SHOW THE EXPANDED SIGNAL BEFORE AND AFTER ENDURANCE TESTING, RESPECTIVELY.



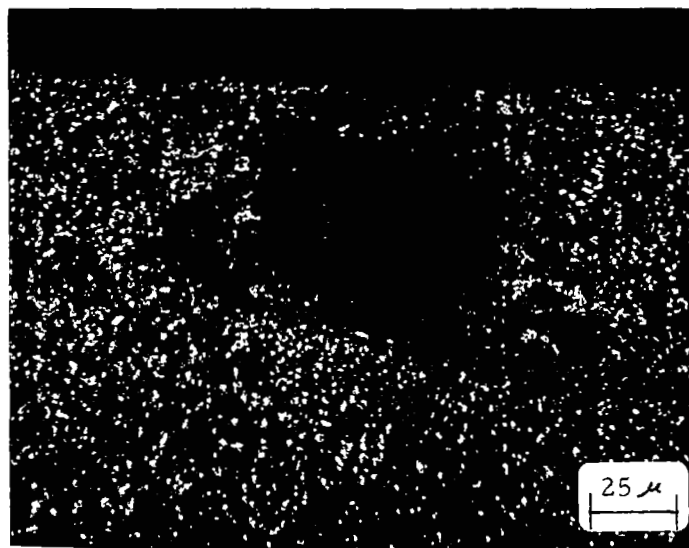
(a)



(b)



(c)



(d)

FIGURE 21. SPECIMEN #85 DEFECT SIGNAL AT 305° AND CORRESPONDING DEFECT. (Note sulfide particles (arrows) about the inclusions in (b) and (c), two sections separated by 12.5μ).

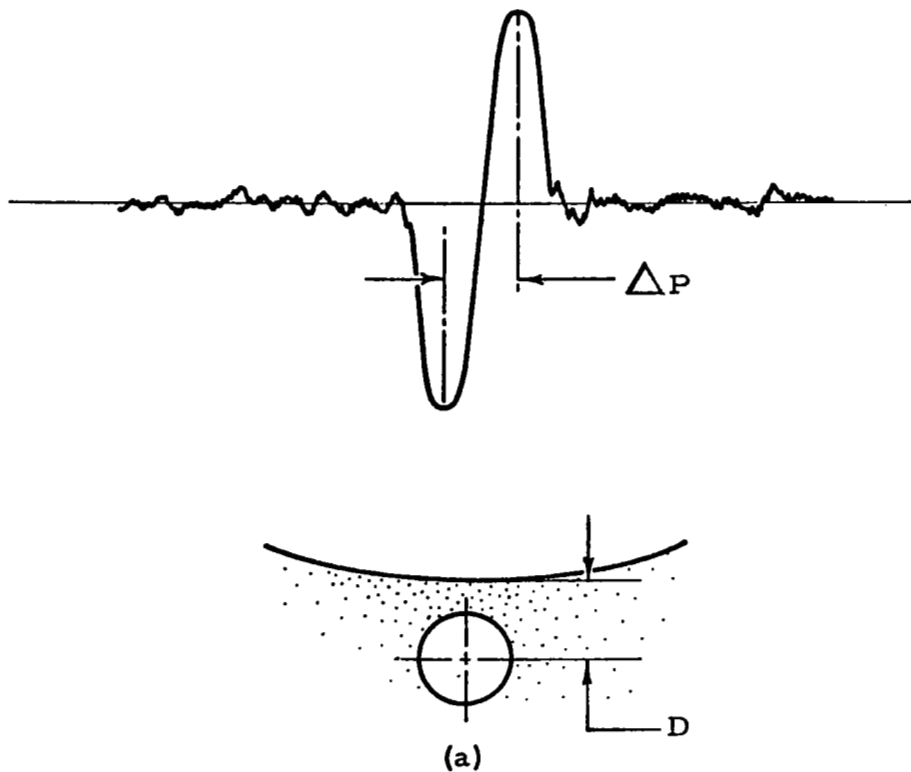
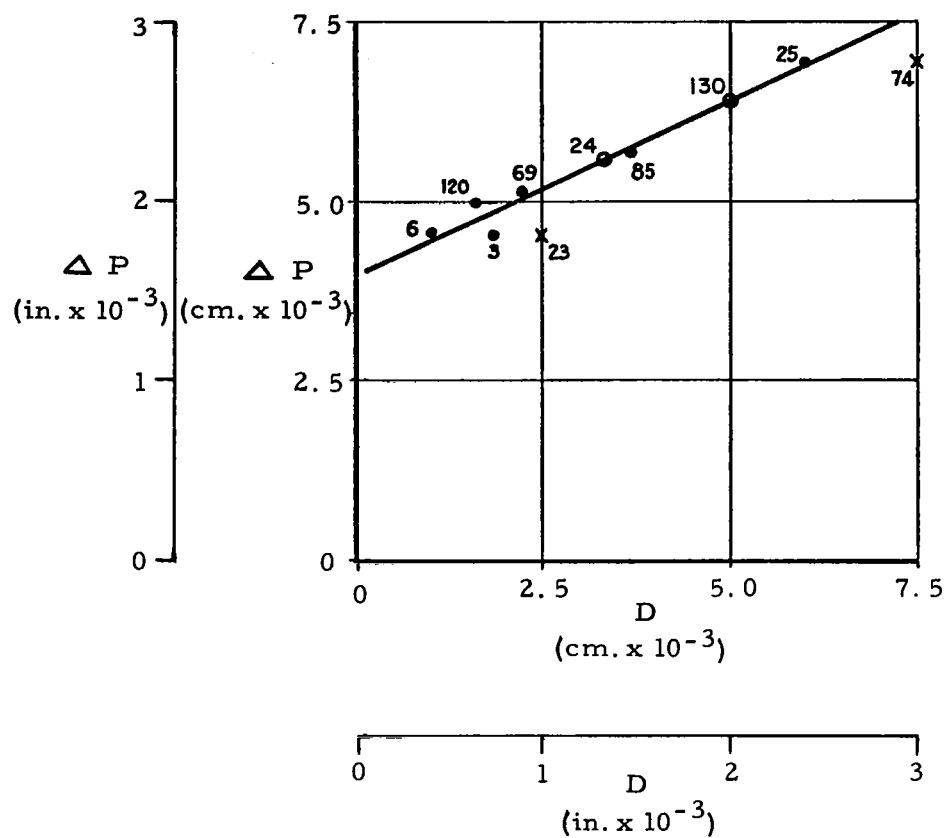


FIGURE 22. (a) SCHEMATIC VIEW OF MAGNETIC PERTURBATION SIGNAL HAVING PEAK SEPARATION ΔP CAUSED BY DEFECT AT DEPTH D



(b)

FIGURE 22. (cont'd) (b) PLOT OF ΔP VERSUS D FOR SEVERAL DEFECTS

4. Surface Damage (Indentations)

In all (13) cases of spalling which could not be traced to subsurface inclusion nucleation, i. e. , excluding specimens 24 and 130, it was observed that initiation of the spalls was caused by surface damage (one or two bearings were damaged so severely that one could not be positive that every spall was caused by an indent rather than a subsurface flaw). This damage always consisted of indentations lying just at the leading edge of each spall, examples of which are shown in Figure 23 (a-b). The direction of ball travel is shown by an arrow. While it is not known precisely at what time these indents were introduced, they definitely were not present following magnetic field perturbation inspection prior to the bearing fatigue tests. It is important to note that a spall will not necessarily nucleate at every indentation formed on a raceway surface.

Where spalls did initiate at indentations, the failure process proceeded as shown in Figure 23 (c-d). Here, microcracks have formed at the trailing edge of local indents. Beneath the surface, the crack profile appears as shown in Figure 24; note that the crack extends only a short distance beneath the surface before leveling off and growing parallel to the raceway surface. Subsequent spalling-out of material produces the macro-failures, or spalls, of Figure 23 (a-b).

In sectioning through spalled regions, two general types of crack configurations were encountered. The first case is shown in Figure 25(a), in which the crack propagates in the absence of any apparent plastically deformed (white etching) zone along the crack interface. Compare this behavior with that shown in Figure 25(b). The reason for this difference is not known, although it is interesting that both types of crack usually lie at an angle of approximately 28° with respect to the bearing surface (See Figure 25(a)). In addition, it appears from photos such as that of Figure 25(a) that the dispersed chromium carbides (white spots) have little or no control over crack growth, since no special carbide configurations are evident along the crack interface.

During sectioning, only a few "butterflies" were encountered; an example of one is shown in Figure 26. It is interesting to note that (1) the "butterfly" is oriented at an angle of approximately 45° with respect to the surface, and (2) the depth of the inclusion is 0.018 cm (0.007 inch), well within the most highly stressed zone. In Figure 26(b), note that cracking within the "butterfly" has begun. This defect was too small ~ 0.005 cm (0.002 inch dia.) and deep to permit magnetic perturbation detection.

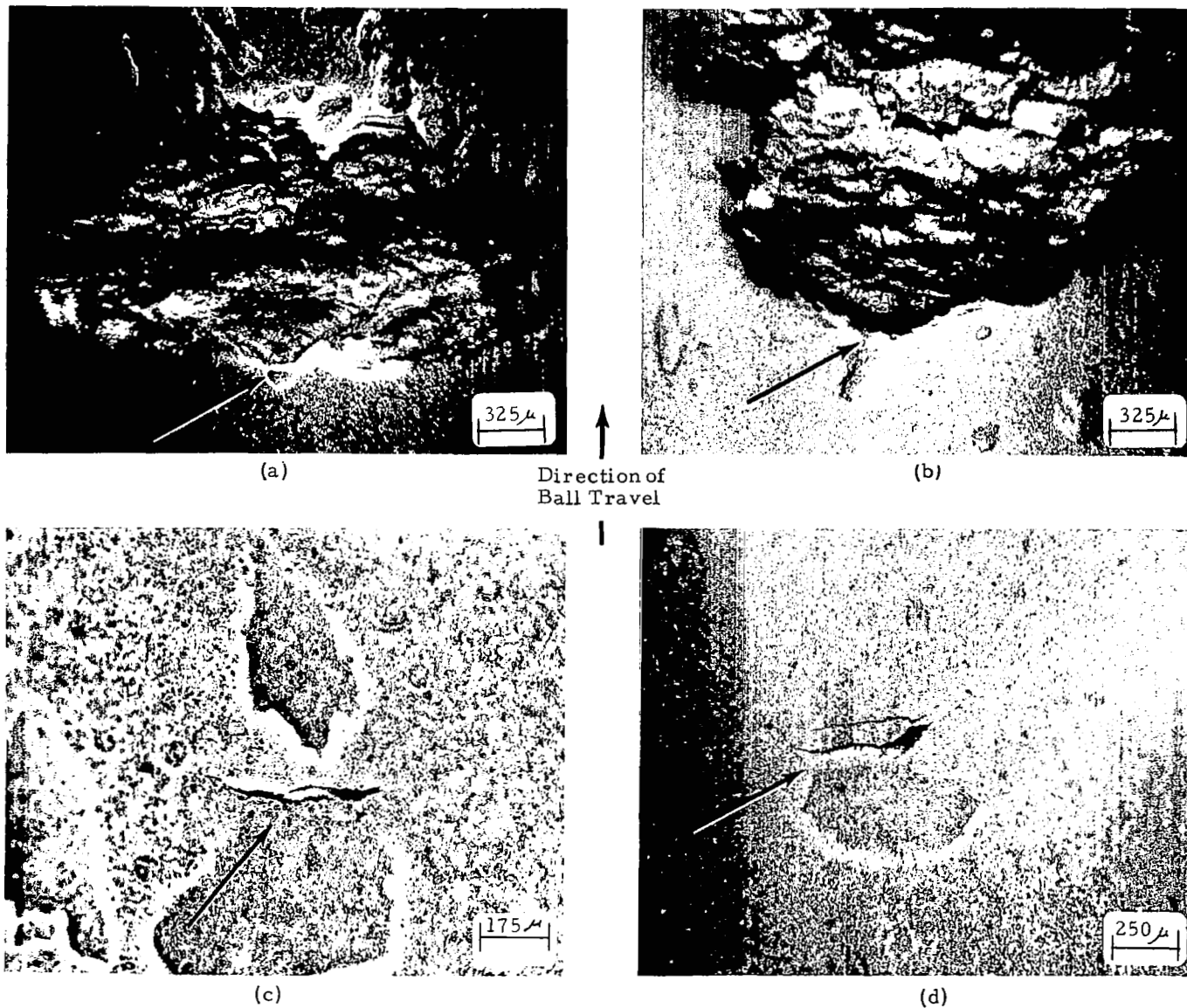


FIGURE 23. SPALLS (a-b) AND PRE-SPALL CRACKING (c-d) AT SURFACE INDENTS. (Arrows indicate spall formation at trailing edge of indents).

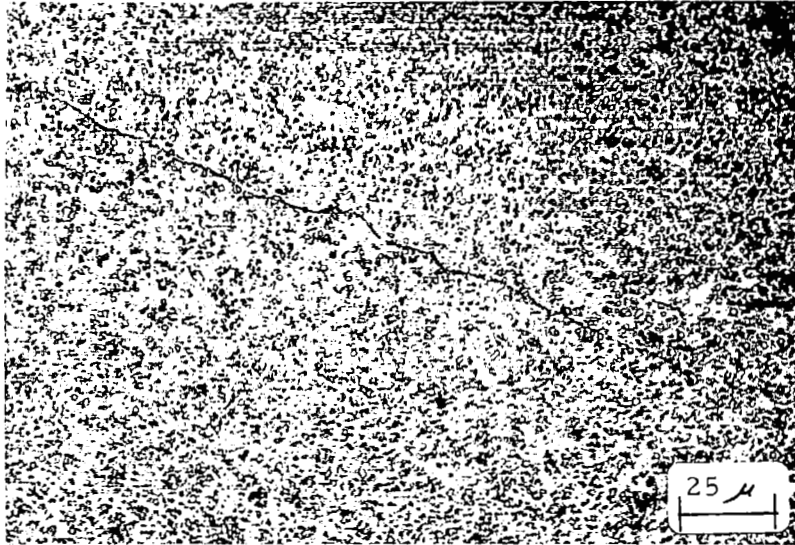


(a)



(b)

FIGURE 24. SECTION THROUGH CRACK AT TRAILING EDGE OF INDENT, (a) UNETCHED, (b) ETCHED. (Situation similar to that of Figure 23 (c-d).)



(a)



(b)

FIGURE 25. SUBSURFACE CRACK CONFIGURATION



(a)



(b)

FIGURE 26. BUTTERFLY FORMED AT INCLUSION, (a) ETCHED, (b) UNETCHED.

5. Plastically Deformed Subsurface Zone

It was anticipated that the apparent shift in rolling track centerline would be reflected in a corresponding shift in position of the zone of plastic deformation usually present in bearings rig-run at high loads. Therefore, some of the sectioned bearings were etched in picral (which helps bring out these zones) and studied in both bright field and polarized light. An example of these zones is shown in Figure 18. From the data of Table I, one would expect to observe the largest plastic zone shift for specimen #74, which exhibited a centerline displacement of 14° . Surprisingly, however, the centroid of the plastic zone shifted only 2° , as shown in Figure 27. It is interesting to observe that the width of the apparent rolling track zone (in degrees) is approximately 2.5 times that of the plastic zone; a typical plastic zone width was $\sim 21^{\circ}$. On the average, the upper edge of the plastic zone at the center of the ball track was about 0.0059 cm (0.0022 inch) deep, while the center of the plastic zone, or most highly strained region, was approximately 0.013 cm (0.0052 inch) below the surface. These estimates are simply inferred of course, from the etching character of the zones.

6. Opposite Polarity Signals

Two specimens (No. 11 and No. 116) having large opposite polarity signals were sectioned in order to establish whether or not the origins of the signals were subsurface inclusions. Initial optical examination of the raceway surfaces in the vicinity of the signal locations had revealed no local surface alterations. The subsequent sectioning operation likewise failed to show any microscopically detectable flaw or anomalous condition, even though the same precision sectioning procedure (used to confirm all void signals) was followed.

7. Tabulation of Data

In the following section, certain important metallurgical factors related to the sectioned bearings are tabulated. In addition, magnetic perturbation parameters related to these physical quantities are listed. The data included consist of:

- (a) Specimen serial number,
- (b) Circumferential and axial location of specific signals,
- (c) Signal amplitude and polarity obtained from the expanded Polaroid records,

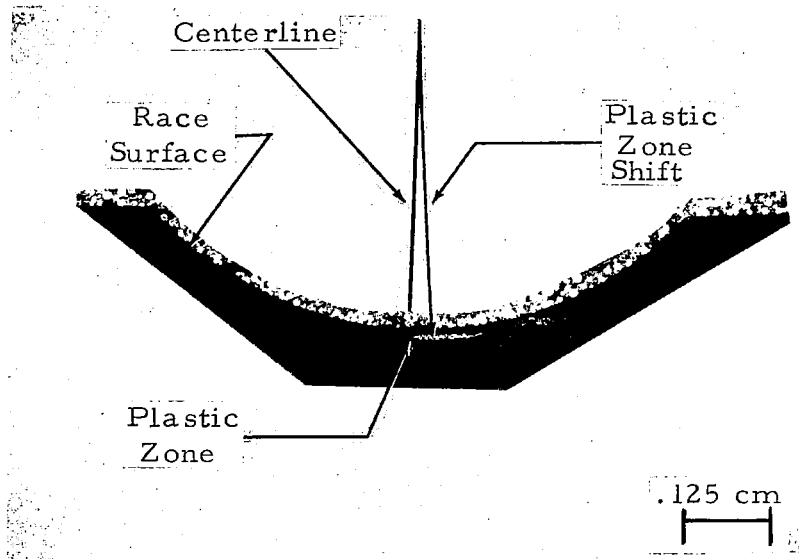


FIGURE 27. SECTION THROUGH BEARING #74 SHOWING PLASTIC ZONE SHIFT OF 2° FROM CENTERLINE OF BEARING

- (d) Signal-to-magnetic background ratio,
- (e) Peak separation,
- (f) Depth of defect relative to raceway surface,
and
- (g) Diameter of defect.

These data are presented in Table III. Note in particular the post-endurance signal amplitudes and signal-to-magnetic background ratios, and compare them with the corresponding pre-run values.

TABLE III

SECTIONING DATA

Ring No.	Angle (°)		Post-Endurance Run			Pre-Endurance Run			Peak	Defect	Defect
			Amp (mV)		Peak/	Amp (mV)		Peak/	Separation	Depth	Size
	Circ.	Axial	Void	Opp.	Background	Void	Opp.	Background	cmx10 ⁻³ (inx10 ⁻³)	cmx10 ⁻³ (inx10 ⁻³)	cmx10 ⁻³ (inx10 ⁻³)
3***	5	3.5	40		1.7/1	39		3/1	4.6 (1.8)	1.9 (0.75)	3.8 (1.50)
6***P	312	347.0	28		2.5/1	53		5/1	4.6 (1.8)	1.0 (0.40)	2.54 (1.00)
23 P	327	7.7	50		2.5/1	22		4/1	4.6 (1.8)	2.54 (1.00)	3.8x6.3x0.5 (1.5x2.5x0.2)
24**	9	7.7	--		--	67		6/1	5.6 (2.2)	--	6.8 (2.70)
25 P	195	352.2	34		1.5/1	30		2.5/1	7.1 (2.8)	6.1 (2.40)	2.8 (1.10)
69 P	50	23.5	44		2/1	38		4/1	5.3 (2.1)	2.16 (0.85)	3.05 (1.20)
74	226	2.5	60		5.5/1	25		2/1	7.1 (2.8)	7.6 (3.00)	2.5x11.5x0.25 (1.0x4.5x0.1)
85	305	347.0	52		4/1	49		7/1	6.1 (2.4)	3.8 (1.50)	7.0 (2.75)
120 P	288	357.5	42		2/1	47		3/1	5.0 (2.0)	1.5 (0.60)	2.3 (0.90)
130**	308	357.5	--		--	58		6/1	6.6 (2.6)	--	--
11 P	315	352.2* -18.2		115	7/1		55	6/1	24.4 (9.6)	--	--
116	55	2.5- 18.2*		92	4.5/1		30	4/1	--	--	--

* Range over which opp. polarity signal persisted.

** Failed at signal.

*** Cracking at inclusion.

P Prestressed during run-in cycles.

III. ANALYSIS

A. Pre-Endurance Testing Data Analysis

Analysis of the initial magnetic inspection records disclosed a total of 23 specimens from the group (103 total) with signals that have usually been associated with voids and/or inclusions. Referring to Table II, these are: 3, 6, 7, 23, 24, 25, 48, 66, 69, 74, 82, 85, 89, 96, 110, 120, 129, 130, 132, 148, 160, 165, and 168. In general, these signals had peak separations of approximately 5×10^{-3} cm (2×10^{-3} inches), and therefore, are caused by sources within approximately 10^{-2} cm (4×10^{-3} inches) of the surface. In the case of specimen No. 6, two separate void polarity signals were obtained on adjacent tracks and at approximately the same circumferential location. In another instance, in specimen No. 7, the signal was somewhat unusual in that a portion of the signal appeared at 263° circumferentially and 2.5° axially with the remainder of the apparent signal at 262° circumferentially and 357.5° axially. It is assumed that this particular signal was located near the junction of the inspection track at 2.5° and at 357.5° , and that the signal source was probably at a slight angle, perhaps 10° to 15° , with respect to the axial centerline of the specimen. Specimen No. 148 had two separate void signal sources.

Since those flaws located in the zones of highest stress are most likely to cause the earlier bearing failures, the data in Table II have been analyzed to determine which specimens were in such a category. This region of highest stress is arbitrarily assumed to be a zone which is ± 0.075 cm (± 0.030 inch) wide on either side of the centerline of the bearing groove. The limiting axial scan track locations for this region are respectively 7.6° and 352.2° . Void signals located outside these limits, on the basis of past experience, have not been nearly as critical as those located within this region. Of course, there is no sharp dividing line, and these limits are established on the basis of a maximum Hertz stress of 3.24×10^9 N/m² (470,000 psi) at the groove centerline. Within these angular limits 12 specimens generated void polarity (inclusion) signals and possibly another one should be included to make a total of 13. Referring to Table II, these specimens are, respectively, 3, 7, 23, 24, 25, 74, 82, 85, 120, 129, 130, 148, and 165. On the basis of past experience involving 208-size bearings, it was likely that these specimens would fail at the void polarity signal source before approximately 200 hours life* provided the specimens were run at a maximum Hertz stress of approximately 3.24×10^9 N/m².

* Based on experimental results obtained in an earlier, unpublished industry-sponsored bearing program.

(470,000 psi) and provided surface indentation damage occurring during running and/or possibly installation damage does not provide a failure source that is more critical. However, the stress level employed during this work was only $2.42 \times 10^9 \text{ N/m}^2$ (350,000 psi), so that it was necessary to calculate a new inclusion-limited life. It was assumed that stress levels and lifetimes are related, approximately through

$$\frac{L_1}{L_2} = \left[\frac{S_2}{S_1} \right]^{10}$$

where L is bearing lifetime and S is stress. Further, it was necessary to correct for different ball complements and RPM. This correction factor f_i was calculated on the basis of

$$f_i = 1/2Z \left[1 + \frac{dw}{dm} \cos \alpha \right]$$

where for 207-size bearings:

$$Z = \text{number of balls} = 9$$

$$dw = \text{ball diameter} = 1.1 \text{ cm (0.4375 inch)}$$

$$dm = \text{mean diameter of ball groove} + \text{ball diameter} = 5.3 \text{ cm (2.1023 inch)}$$

$$\alpha = \text{contact angle} = 0^\circ \text{ for radial loading.}$$

Employing this calculation, one finds

$$\frac{L_{207}}{L_{208}} = \frac{1}{1.4} \left[\frac{S_{208}}{S_{207}} \right]^{10}$$

which can be used to predict that inclusion nucleated failure, in 207-size bearings under present test conditions, should occur not before 500 hours and not after 2100 hours*.

Several specimens with opposite polarity signals were examined, for example, 11, 12, 15, 115, 116, and 136. It was not anticipated that these specimens would fail at the signal sources causing the rather outstanding opposite polarity signals. In general, these

* Ibid.

opposite polarity signals had much "broader" peak separations, for example, specimen No. 11 had a peak separation of 2.4×10^{-2} cm (9.6×10^{-3} inches), and past experience has not disclosed discrete flaws as being the source of such signals. Furthermore, since these signals extended for an appreciable distance across the race groove, there is a basis for suggesting that the fiber orientation in some manner causes such signals. In general, these signals are not considered to be of significant influence in bearing failure.

B. Post-Endurance Testing Data Analysis

There is a remarkable correlation between magnetic perturbation signatures and metallurgical sectioning results. Specifically, each void signature region examined disclosed an inclusion.

A preliminary appraisal indicates only a limited correlation between endurance test failures and magnetic perturbation signatures. Only two specimens of the 12 with such signatures failed; with the exception of these two, all other failures (spalls) occurred at surface indents. A detailed appraisal, however, indicates that a rather striking correlation exists when inclusion location, size, relation to stress affected zone, etc., are considered. The following discussion clarifies this assertion.

It is useful at this point to consider the results of the inspection, endurance testing, and sectioning in terms of actual and potential inclusion-related failure. During the following discussion it will be extremely useful to refer to Table III and to Figure 28. The latter figure shows the locations, relative size, and depth of the inclusions located during metallurgical sectioning, relative to the race surface and to the subsurface plastically deformed zone.

Two of the specimens, numbers 24 and 130, experienced spall nucleation at large amplitude void-polarity signals. It is interesting to note that aside from that of specimen No. 85, the defect signal-to-background ratios for the above two inner races were the largest recorded, i. e., 6:1. Of greater importance was the fact that the absolute signal amplitude, which is related to flaw size, was 67 mV for No. 24 and 58 mV for No. 130. Not only were these the two largest signals, but the axial locations (7.7° and 357.5° , respectively) were well within the highly stressed zone covering $\pm 10.5^\circ$, shown in Figure 28. Further, recalling Figure 22(b), it is possible to calculate the apparent depth of the defects corresponding to these two signals,

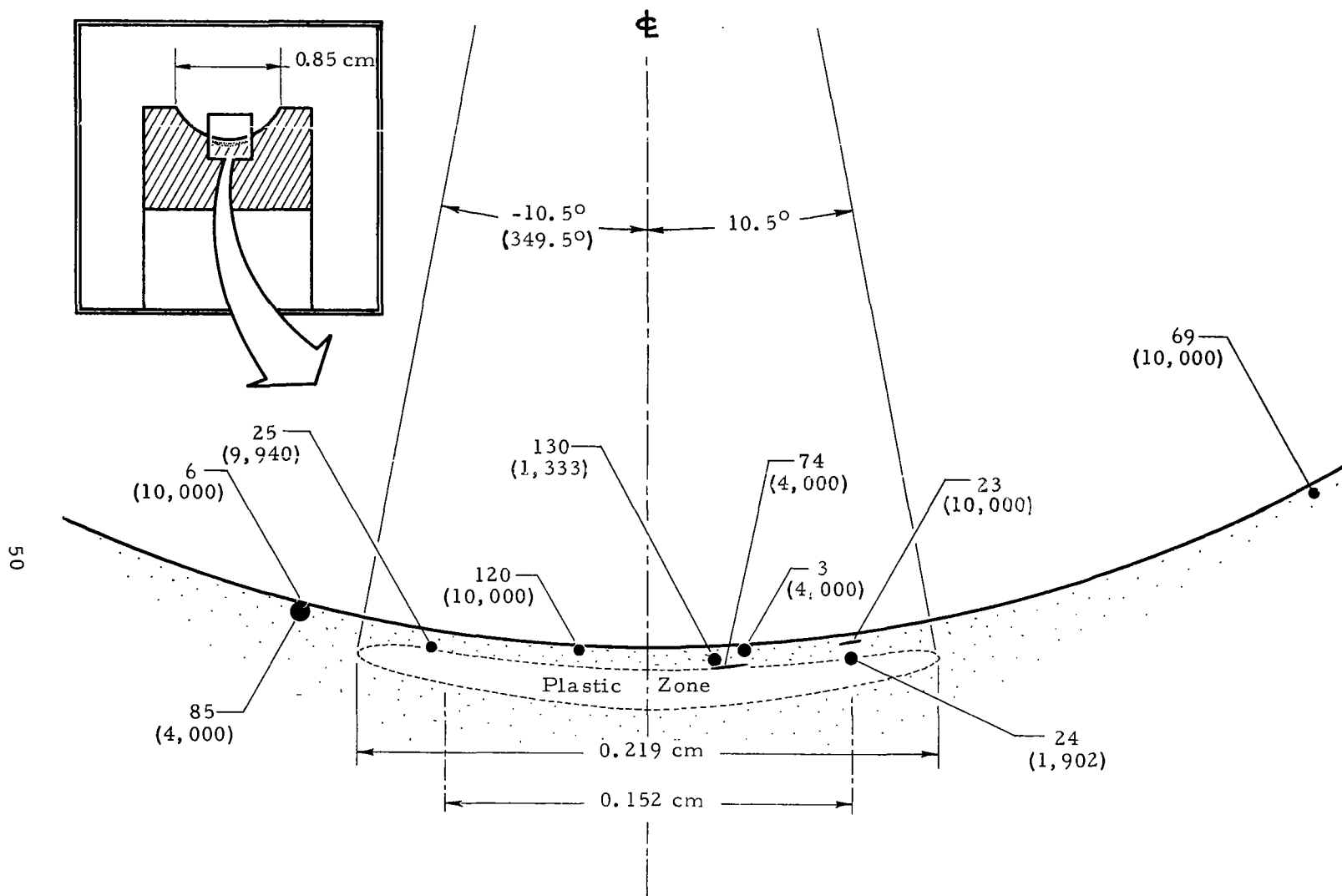


FIGURE 28. SCHEMATIC SHOWING DEFECT LOCATIONS AND SUBSURFACE PLASTIC ZONE
(Lifetimes in hours listed as subscripts)

as indicated by the open circles plotted on the experimental curve, for the observed peak separations. Note that the defect which caused specimen No. 130 to fail was probably deeper than that responsible for the spalling of No. 24. In general, one would have expected No. 130 to develop severe plastic deformation and microcracking sooner than No. 24, since it would have been closer to the region of maximum orthogonal shear stresses, which lay approximately 0.012 cm (0.005 inch) below the surface, on the basis of etching characteristics. Specimen No. 130 apparently just entered the upper edge of the plastically deformed subsurface zone at the 0.0056 cm (0.0022 inch) depth, which No. 24 did not. It is significant, then, that the former specimen failed after only 1333.3 hours, yet No. 24 survived for 1902.7 hours, half again as long.

Since specimens 24 and 130 provided the most dramatic evidence of the potential inherent in magnetic perturbation inspection of bearings, these two cases are shown pictorially in Figures 29 and 30. Note in particular (Figure 29) the 0.0069 cm (0.0027 inch) diameter nucleating inclusion, preserved within the spall region, which caused the failure of specimen No. 24. This inclusion could be viewed effectively only by means of polarized light. Although the inclusion responsible for nucleating the failure shown in Figure 30 apparently was lost during some phase of spalling, there obviously exists excellent correlation between the signal site at 308° and the leading edge of the spall. Close optical inspection of the leading edges of both spalls (24 and 130) showed no evidence of indentation.

The next largest signal (absolute amplitude 53 mV) was associated with specimen No. 6; this defect (Figure 15) was particularly interesting, in that it touched the surface, and possibly would have resulted in a bearing failure in the event of longer running time. A slight darkening of the etched microstructure is evident near the inclusion. Note also that the inclusion was located axially at 347° , well outside the high stress zone.

Because of the high signal amplitude (49 mV) and signal-to-background ratio associated with No. 85, one might have suspected damage at this site. However, three factors mitigate against this supposition. First, the measured depth of the inclusion was only 0.003 cm (0.0012 inch), although its size was equal to the defect which caused No. 130 to fail. Close inspection using polarized light, however, indicates that this inclusion was partially surrounded by sulfide, and that associated with it were several smaller sulfide particles (arrows in Figure 21). This second factor may help explain the lack of microcrack

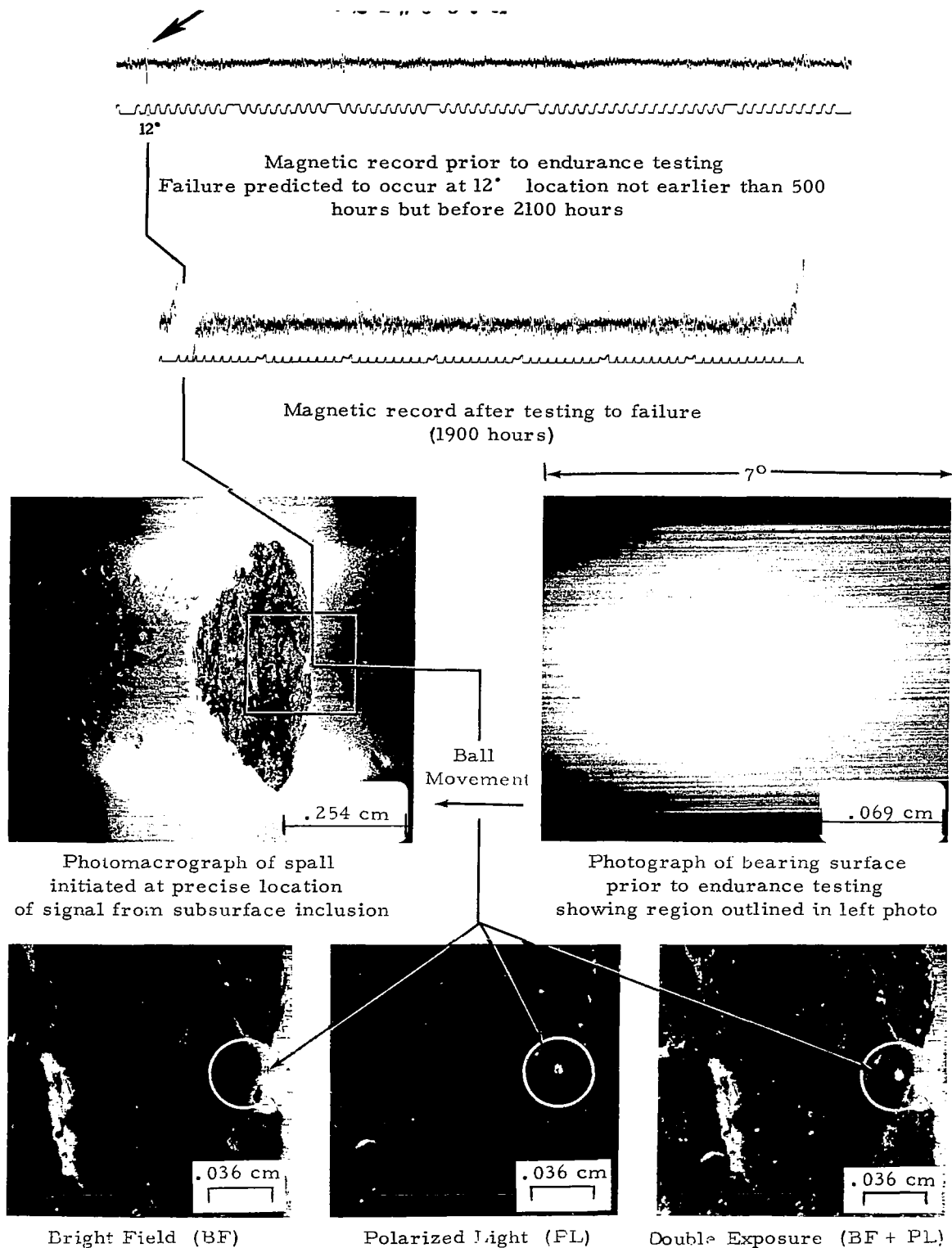


FIGURE 29. LIFE PREDICTION - FAILURE INITIATED AT SUBSURFACE INCLUSION

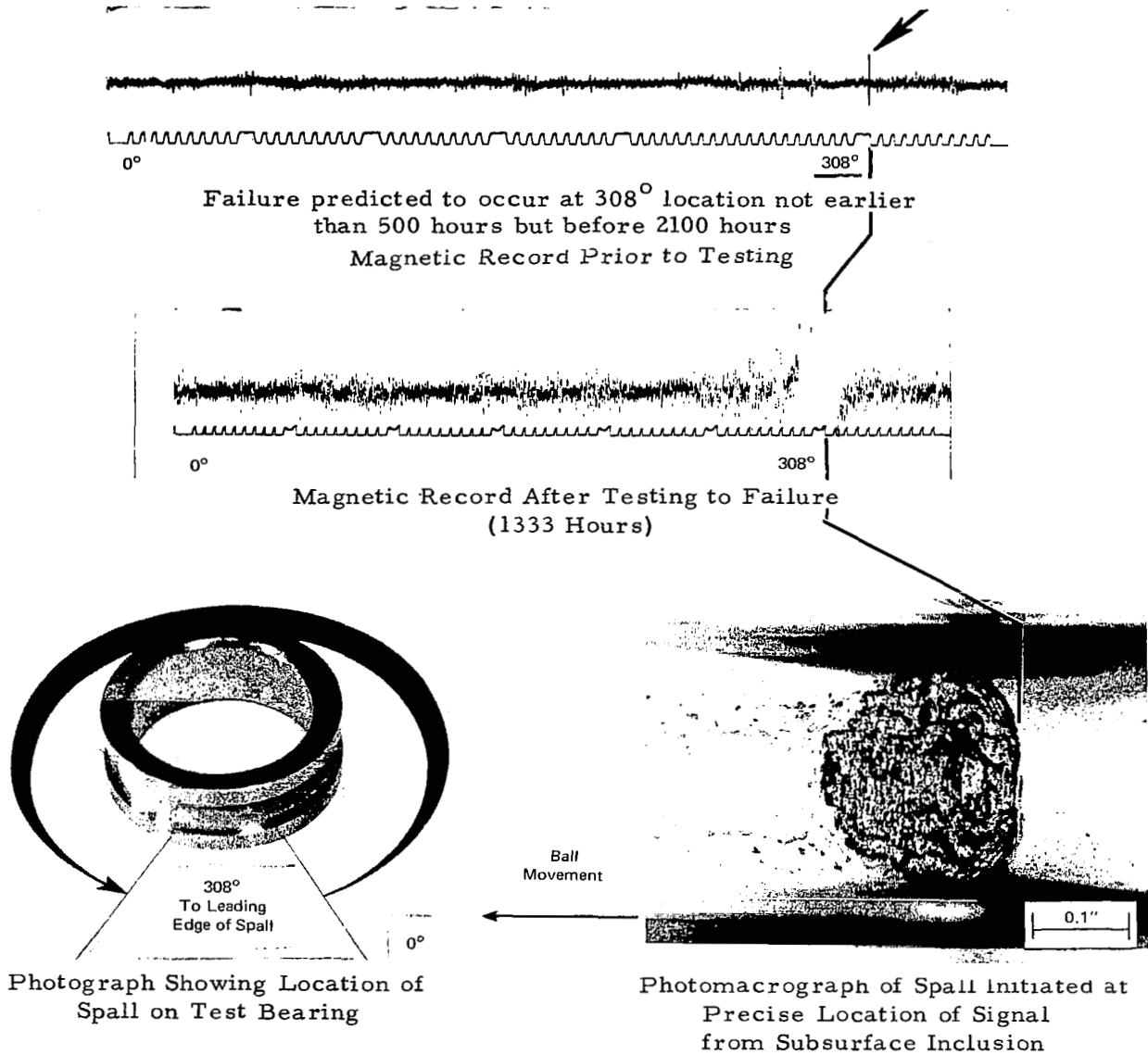


FIGURE 30. SPALL AT PREDICTED SITE IN BEARING #130

evidence at the defect location. Perhaps of dominant importance is the axial location at 347° , well outside the nominal bounds of the highly stressed zone.

The inclusion of specimen No. 3, shown in Figure 14, produced a relatively moderate sized signal of 39 mV. However, no sulfide shell is present, the particle constitutes a good stress raiser, and cracks already have begun to form at 4,000 hours. It is interesting to note that this inclusion is near the center of the ball track, but is considerably smaller than the inclusion in failed specimen No. 24. Despite the presence of microcracks, no deformation-induced etching alteration is evident in Figure 14(d). Note from Table II that specimen Nos. 3 and 6, both quite shallow in depth, generated defect signals having the minimum peak separation of 4.8×10^{-3} cm (1.8×10^{-3} inch).

Two other particularly interesting specimens were numbers 23 and 74. In each of these cases, the defects detected turned out to consist of planar sulfide sheets containing slender, rodlike silicate or aluminate "backbones," which may help explain the unique signal amplitude increases observed in these two cases. Figure 16 shows three sections through the defect of No. 23; a conceptual sketch of the particle may be seen in Figure 31. No cracks are visible at either inclusion site, indicating either that (1) soft inclusions are inefficient stress raisers, or (2) planar particles are more compatible with high rolling-contact stresses than are volume-equivalent spherical particles. The circumferential angles (2.5° and 7.7°) were such that shear stresses should have been quite high. The flaw in specimen No. 23 caused a 22 mV signal and in No. 74, a 25 mV signal; these are approximately the signal amplitudes associated with Nos. 24 and 130.

The defect of specimen No. 25 is rather interesting when compared with that which initiated the failure of No. 24. Both defects lie at the same equivalent axial position; No. 24 was 0.0069 cm (0.0027 inch) in diameter, while No. 25 measured 0.0028 cm (0.0011 inch); depths, on the basis of peak separation, were approximately equivalent; No. 25 lasted for 9,940 hours before the outer race finally failed, yet No. 24 failed at 1,902 hours at the defect site. Furthermore, No. 25 was essentially a duplex inclusion, i. e., an oxide a silicate particle sheathed within a sulfide. Since both radial and hoop matrix stresses increase with the volume of the inclusion, it is not so surprising that No. 25 should have a greater life expectancy. Further supporting this view is the association of the sulfide with No. 25; Brooksbank and Andrews³ have shown analytically that the presence of such soft

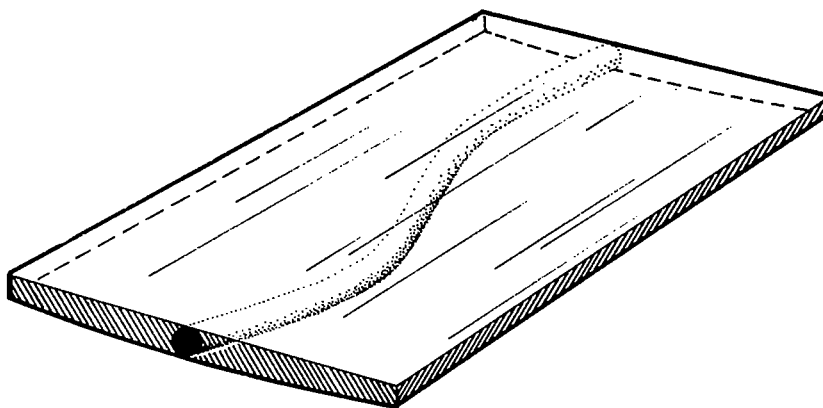


FIGURE 31. PLANAR DUPLEX INCLUSION, SHOWING SILICATE OR ALUMINATE "BACKBONE" WITH SULFIDE SHEET.

"shells" may reduce the calculated matrix by a large factor (as much as 70% for a 2μ thick shell of CaS about a 8μ $\text{CaO} \cdot 2\text{Al}_2\text{O}_3$ particle). In addition, Lyne and Kasak⁴ have produced statistical experimental evidence indicating that sulfide encapsulation has a very real effect in reducing stress concentrations and prolonging fatigue life.

From the data of Figure 22(b), it is apparent that the linear relationship between ΔP and depth may constitute a powerful method for assessing the damage potential of a given defect. Whether or not an inclusion lies sufficiently deep to be affected by the subsurface (Hertzian) plastic zone may have a strong influence on its relative propensity for crack nucleation although this point still is subject for conjecture, and requires further study. It was previously noted that butterflies were observed only in those instances wherein the nucleating inclusion lay within the plastic zone (Figure 26), while microcracking was observed both above (near-surface) and within the plastically deformed region.

From the results of sectioning through the spalled regions, several observations are possible. First, indentation nucleated spalling produces no observable alteration in the character of the subsurface plastic zone (as determined from etching behavior). Subsurface microcracking from such spalls seldom shows any tendency toward the generation of "white etching" microstructure while some of the microcracks emanating from each of the two inclusion-initiated spalls were bound by "white-etching" material. Carbides appeared to play no role in determination of local crack growth direction.

It was not possible to determine whether opposite polarity signals were microstructural or surface-generated in nature. They appeared, however, to have no detrimental effect upon bearing life or structural integrity. The increase in signal amplitude with fatigue cycling may indicate that these signals are metallurgical in nature, hence subject to the same influence as the general magnetic background, which rose somewhat during the cycling.

IV. CONCLUSIONS

- (1) For the material and specimen geometry tested, there existed a remarkably high correlation between signal character and inclusion size and location.
- (2) This correlation was sufficient to allow inferences concerning defect size and depth.
- (3) Under known conditions of running, it is reasonable to predict life-to-failure.
- (4) The two most outstanding signatures, in terms of absolute signal amplitude, corresponded precisely with the only observed inclusion nucleated failures.
- (5) The number of failures other than those initiated at surface indentations were so sparse (2) that conclusions concerning failure criteria at other inclusion locations cannot yet be drawn.

REFERENCES

1. Todd, F. C. , and Donaldson, W. L. , "Non-Destructive Testing of Ball Bearing Components, " New Departure Report Nr. 672-6, July, 1957.
2. Fogwell, J. W. , Kusenberger, F. , and Donaldson, W. L. , "Nondestructive Evaluation of Metal Fatigue, " Southwest Research Inst. Report AFOSR-64-0668, AD-600277, March, 1963.
3. Brooksbank, D. , and Andrews, K. W. , "Stresses Associated with Duplex Oxide-Sulphide Inclusions in Steel, " Journal of the Iron and Steel Institute, June, 1970, 582.
4. Lyne, C. M. , and Kasak, A. , "Effect of Sulfur on the Fatigue Behavior of Bearing Steel, " Transactions of the ASM, 61, 1968, 10.